Journal of Sound and Vibration 576 (2024) 118268

Contents lists available at ScienceDirect

Journal of Sound and Vibration

journal homepage: www.elsevier.com/locate/jsvi

Topological localized modes in moiré lattices of bilayer elastic plates with resonators

Tamanna Akter Jui, Raj Kumar Pal *

Department of Mechanical and Nuclear Engineering, Kansas State University, Manhattan, KS, 66506, USA

ARTICLE INFO

Keywords:
Higher order topology
Localized mode
Moiré
Twisted
Elastic
Plane wave expansion method (PWEM)
Fractional corner mode

ABSTRACT

We investigate the existence of higher order topological localized modes in moiré lattices of bilayer elastic plates. Each plate has a hexagonal array of discrete resonators and one of the plates is rotated at an angle (21.78°) which results in a periodic moiré lattice with the smallest area. The two plates are then coupled by inter-layer springs at discrete locations where the top and bottom plate resonators coincide. Dispersion analysis using the plane wave expansion method reveals that a bandgap opens on adding the inter-layer springs. The corresponding topological index, namely fractional corner mode, for bands below the bandgap predicts the presence of corner localized modes in a finite structure. Numerical simulations of frequency response show localization at all corners, consistent with the theoretical predictions. The considered continuous elastic bilayered moiré structures opens opportunities for novel wave phenomena, with potential applications in tunable energy localization and vibration isolation.

1. Introduction

The study of architected two-dimensional ($2D$) moiré lattice structures has gained a lot of attention, particularly in $2D$ materials. Moiré lattices are formed when one periodic lattice is rotated with respect to another identical lattice, see Fig. 1 for an example. At specific angles of rotation/twist, a lattice with a larger periodicity results, called the moiré lattice. Their dispersion surfaces have unique features like flat bands, and nonlinear (interacting) inter-layer coupling effects that enable various exotic phenomena [1–5]. Notable examples include recent breakthroughs with twisted bilayer graphene, including high-temperature super-conductivity [6] and two-dimensional magnetism [7].

These recent discoveries in quantum mechanics have inspired the quest for novel wave phenomena with moiré structures in diverse physical domains. The ability to independently engineer the rotation angle and inter-layer interactions, combined with advances in fabrication have opened a rich design space. Examples in photonics include flat bands using a hexagonal array on silicon nanodisk [8], lasing by semiconductor membrane with a triangular pattern of nanoholes [9], topologically protected corner modes [10], and localization–delocalization transition of light [11]. These phenomena arise solely due to the relative rotation between two lattices, without introducing any structural defect, material discontinuity, or non-linearity. Similarly, in acoustics, bilayer moiré structure made of coupled acoustic cavities in various lattice configurations has been investigated. It has led to higher-order topological states (HOTI) with hexagonal lattice [12], acoustic valley edge modes with triangular [13] and topological Lifshitz transition with square lattice [14].

In elastic media, the presence of both longitudinal and shear (transverse) waves offers rich possibilities for novel dynamic phenomena with architected structures. Recent studies have investigated the dynamic properties of moiré lattices comprising of

* Corresponding author.
E-mail address: rkpal@ksu.edu (R.K. Pal).

https://doi.org/10.1016/j.jsv.2024.118268
Received 6 October 2023; Received in revised form 22 December 2023; Accepted 14 January 2024
Available online 22 January 2024

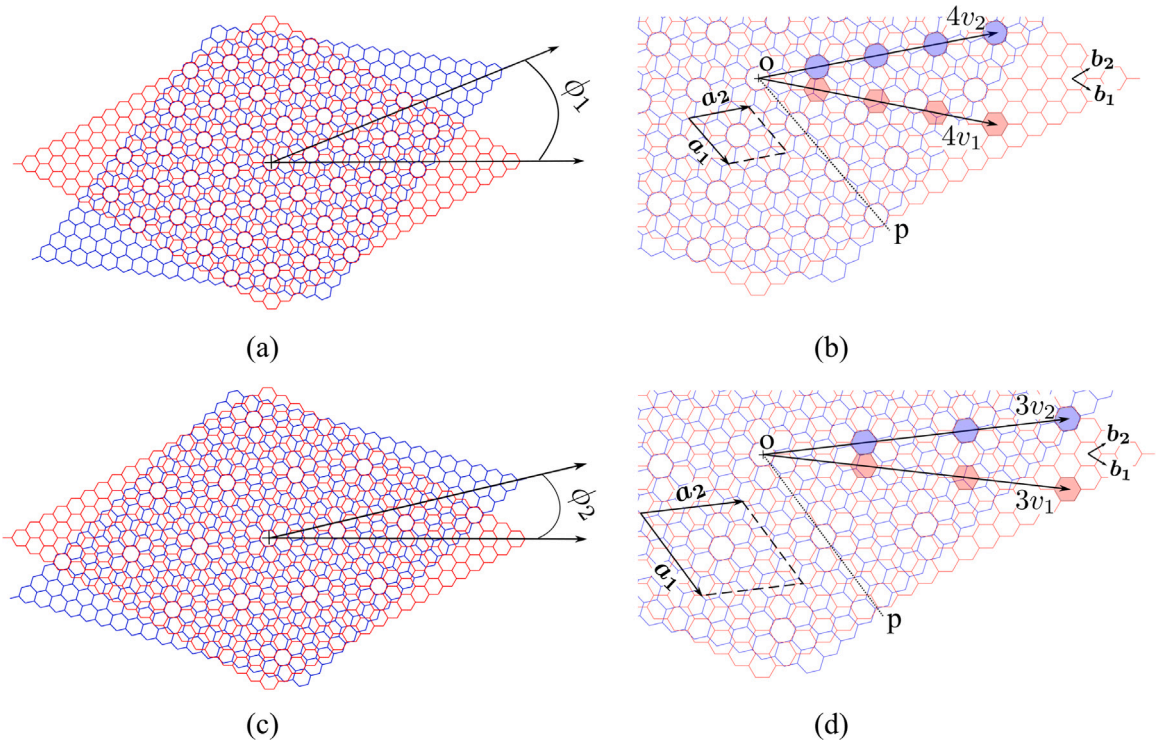

Fig. 1. Schematic of periodic moiré lattices and unit cell. The rotation angle is $\phi_1 = 21.78°$ in (a) and $\phi_2 = 13.17°$ in (c). (b,d) Enlarged view of the lattices, along with lattice vectors. The blue and red shaded hexagons overlap when the two lattices coincide (at $\phi = 0$). The moiré lattice in (a,b) has the smallest unit cell. (For interpretation of the references to color in this figure legend, the reader is referred to the web version of this article.)

elastic plates with arrays of pillars in various configurations. Notable predictions include the existence of non-trivial topological bandgap supporting edge states [15], chirality-driven flat bands analogous to twisted bilayer graphene [16,17] and localized modes [18]. Oudich et al. [19] systematically examined the effect of inter-layer coupling in bilayer pillared elastic plates in a twisted honeycomb arrangement. Their calculations predict that a weak coupling gives a dispersion band structure similar to the classical bilayer graphene, while a stronger coupling induces the valley Hall effect for elastic wave propagation. Ruzzene and coworkers studied single-layer elastic plate moiré structures having a square array of pillars with spatial modulation of heights. They demonstrated a topological transition of isofrequency contour and highly directional wave tunability [20]. A majority of these studies have been conducted on large lattices which are difficult to fabricate. In addition, the nonlinear properties of these lattices remain unexplored. The exotic properties of moiré structures in electronic media listed above are associated with non-linear or interaction effects of spectrally isolated bands and localized modes. Hence similar localized modes may give rise to analogous nonlinear phenomena in elastic media.

Although localized modes have been extensively investigated in architected structures over the last few decades, recent research has focused on modes that arise due to nontrivial dispersion band topology. Their topological origin guarantees their existence and they are immune to structural defects and imperfections. In contrast to accidental or trivial localized modes, topological modes translate across geometric parameters, length scales and material properties. Hughes and coworkers [21,22] developed the theory to establish the topological nature of localized modes at corners and point defects in higher dimensional lattice structures and derived the invariants to systematically infer their presence. Topological localized modes have been observed in diverse physical domains, including photonic [10,23–29], acoustic [30–34], phononic [35–37], and elastic [38–41]. They have also been predicted in moiré lattices of twisted bilayer graphene with various inter-layer potentials, however there is disagreement between the various predictions on their locations. Liu et al. [42] show the localized mode only at the 120° corner and provide symmetry-based reasons for non-existence of such modes at a 60° corner, while Wu et al.predict them at both 60° and 120° corners [12].

Here, we investigate the existence of such topological corner localized modes in bilayer elastic moiré plates. We consider two elastic thin plates having a hexagonal array of resonators. The plates are rotated at an angle (21.78°) relative to each other to generate a moiré pattern. Discrete inter-layer springs are added between the plates at locations where the top and bottom plate resonators coincide. The dispersion spectrum and fractional corner mode are determined for a unit cell to predict the existence of corner localized modes. The predictions are verified through numerical simulations of frequency response on a finite plate. The outline of this paper is as follows: Section 2 presents the lattice configuration and the governing equations, followed by a dispersion analysis and computation of topological indices for a unit cell in Section 3. The numerical results of mode shapes and frequency response are presented in Section 4 and the results are summarized in Section 5.

2. Lattice description and problem setup

We first derive the conditions that result in a periodic hexagonal moiré lattice, determine the smallest such lattice and its lattice vectors. Then the elastic plate configuration and its governing equations are presented.

2.1. Lattice and unit cell: geometric description

Fig. 1 displays examples of hexagonal moiré lattices, along with their unit cells and lattice vectors. They are formed by stacking two identical hexagonal lattices with a relative rotation between them. The rotation is about the center of a hexagon with respect to its out-of-plane axis. The blue and red lattices are identical, but rotated relative to each other about O. The lattice vectors of the red hexagonal lattice are $\boldsymbol{b_1}$, $\boldsymbol{b_2}$ with 60° angle between them, and the unit cell length is b. For an arbitrary relative rotation, the resulting pattern is not periodic. At specific rotation angles, a periodic pattern does result. These angles are hereby called moiré angles.

Let us discuss the conditions under which a periodic moiré lattice arises. We analyze the configuration that results when the blue lattice, which is initially coincident with the red one, is rotated about O. Two videos are presented in the supplementary materials on this rotation, illustrating the formation of the two distinct moiré lattices of Fig. 2(a,c). Let us fix this rotation center O as the origin of our coordinate system. The key observation is that a periodic moiré lattice results when the center of a hexagon in a blue lattice coincides with the center of another hexagon in a red lattice away from the origin. The distance between the hexagon center and the rotation center O should be identical for a pair of hexagons, one each from the blue and red lattice. Let us consider a hexagon in the red lattice with center $\boldsymbol{v}_1$ at

$$\boldsymbol{v_1} = m\boldsymbol{b_1} + n\boldsymbol{b_2}, \quad m, n \in \mathbb{Z}, \quad m > n, \quad \gcd(m, n) = 1. \tag{1}$$

Its distance from the center is $\|\boldsymbol{v_1}\| = b\sqrt{m^2 + mn + n^2}$. It is the nearest red shaded hexagon from the center in the examples in Fig. 1(b,d). Due to the C_6 (6-fold rotation) symmetry of the hexagonal lattice, there are multiple hexagons in the blue lattice at the same distance. A simple choice for a hexagon in the blue lattice is $\boldsymbol{v_2} = n\boldsymbol{b_1} + m\boldsymbol{b_2}$, which satisfies $\|\boldsymbol{v_1}\| = \|\boldsymbol{v_2}\|$. The rotation angle (moiré angle) ϕ is thus the angle between $\boldsymbol{v_1}$ and $\boldsymbol{v_2}$, given by

$$\cos\phi = \frac{\boldsymbol{v_1}.\boldsymbol{v_2}}{\|\boldsymbol{v_1}\|\|\boldsymbol{v_2}\|} = \frac{m^2/2 + n^2/2 + 2mn}{m^2 + n^2 + mn}. \tag{2}$$

Let us see why the resulting bilayered (moiré) lattice is periodic along 2 directions and derive the lattice vectors of its unit cell. Note that any integer multiple of $\boldsymbol{v_1}$, i.e., $q\boldsymbol{v_1}$ is also the center of a hexagon in the red lattice. In addition, this hexagon goes to $q\boldsymbol{v_2}$ after rotation, as the angle between $q\boldsymbol{v_1}$ and $q\boldsymbol{v_2}$ is also ϕ. Thus the lattice is periodic along $\boldsymbol{v_2}$, with periodicity $\|\boldsymbol{v_2}\|$. Since both the hexagonal lattices have C_6 (6-fold rotation) symmetry about O, the combined lattice also has C_6 symmetry about O. The moiré lattice is thus also periodic along directions at angle $\pi/3$ from $\boldsymbol{v_2}$. We take its lattice vectors to be $\boldsymbol{v}_2$ and a vector at angle $-\pi/3$ from $\boldsymbol{v}_2$. In terms of the hexagonal lattice vectors, the moiré lattice vectors $(\boldsymbol{a}_1, \boldsymbol{a}_2)$ may be expressed as

$$\boldsymbol{a}_1 = n(\boldsymbol{b_1} - \boldsymbol{b_2}) + m\boldsymbol{b_1} = (m + n)\boldsymbol{b_1} - n\boldsymbol{b_2}, \quad \boldsymbol{a_2} = n\boldsymbol{b_1} + m\boldsymbol{b_2}. \tag{3}$$

Fig. 1(a,c) displays the periodic moiré lattices for $(m, n) = (2, 1)$ and $(3, 2)$. Their corresponding unit cells and lattice vectors are indicated in Fig. 1(b,d). The relative angles between the blue and red lattices for these lattices are $\phi_1 = 21.78°$ and $\phi_2 = 13.17°$. The blue and red shaded hexagons coincide when there is no relative rotation between the two lattices. As the blue lattice is rotated, the blue shaded hexagons move to the locations illustrated in the figure, and they lie along $\boldsymbol{v_2}$. The lattice vector $\boldsymbol{a_1}$ lies along the line labeled OP. Note from these examples that the unit cell size of the resulting lattice is, in general, different for different ϕ values.

In this work, we investigate the behavior of the lattice with the smallest moiré unit cell, due to its potential ease of fabrication with macro-scale components. To determine this unit cell, let us calculate the unit cell area A for a lattice with unit vectors given by Eq. (3). It is given by

$$A = \|\boldsymbol{a_1} \times \boldsymbol{a_2}\| = \frac{\sqrt{3}b^2}{2}\left(m^2 + mn + n^2\right) = \frac{\sqrt{3}b^2}{4}\left(m^2 + n^2 + (m + n)^2\right). \tag{4}$$

For m and n distinct non-zero integers, a direct calculation shows that $A = 7\sqrt{3}b^2/2$ is the minimum area for $m = 2$, $n = 1$. The lattice vectors are thus

$$\boldsymbol{a_1} = 3\boldsymbol{b_1} - \boldsymbol{b_2}, \quad \boldsymbol{a_2} = \boldsymbol{b_1} + 2\boldsymbol{b_1}. \tag{5}$$

Let us discuss the key properties of this lattice. The parallelogram with lattice vectors labeled in Fig. 1b displays the chosen unit cell, with the center of the hexagon at its center. This choice ensures that a finite-sized hexagon-shaped lattice will have 6-fold rotation symmetry. This property will be used later in Section 3.2 to predict localized modes at corners. This unit cell has 14 nodes of the hexagonal lattice in each layer. Indeed, note that the underlying hexagonal lattice has 2 nodes per unit cell and its area is $\sqrt{3}b^2/2$. Comparing with the moiré unit cell area, we see that the latter is 7 times larger and it thus has 14 nodes. In addition, there are two nodes in each unit cell where the red and blue lattices coincide. These nodes are indicated by green circles in the inset of Fig. 2a. Their locations within the unit cell, with respect to the lower 60° in this inset, are given by

$$\boldsymbol{p_1} = \boldsymbol{b_1} + \frac{\boldsymbol{b_1} + \boldsymbol{b_2}}{3}, \quad \boldsymbol{p_2} = 2\boldsymbol{b_1} + \frac{2}{3}\left(\boldsymbol{b_1} + \boldsymbol{b_2}\right). \tag{6}$$

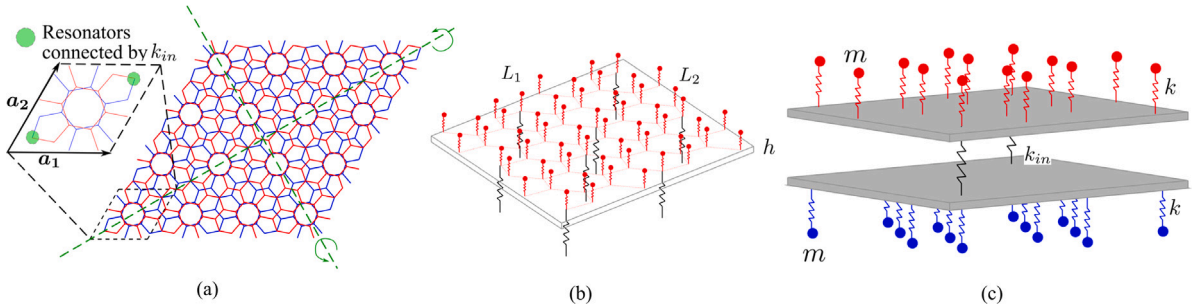

Fig. 2. Schematic of bilayer elastic plate lattice. (a) Moiré lattice with a unit cell in the inset. Green circles indicate locations of coincident resonators in the two layers. Lattice has C_2 symmetry with respect to both its diagonals (green dash lines). (b) Top plate with resonators (red) in hexagonal lattice configuration. Black springs are at the coincident locations indicated in (a). (c) The moiré structure has two plates with resonators, and are coupled by the inter-layer springs, k_{in}. (For interpretation of the references to color in this figure legend, the reader is referred to the web version of this article.)

By checking explicitly, we note that $\boldsymbol{p_1}$ and $\boldsymbol{p_2}$ lie at different sub-lattice sites of each hexagonal lattice. In particular, $\boldsymbol{p_1}$ lies at the α (β) site in the red (blue) lattice, while $\boldsymbol{p_2}$ lies in the β (α) site. Thus the α (β) site of the red (blue) lattice coincides with the β (α) site of the red lattice at $\boldsymbol{p_1}$ ($\boldsymbol{p_2}$) in each unit cell.

2.2. Plate configuration and governing equations

We consider two thin infinite homogeneous and isotropic elastic plates supporting flexural (out-of-plane) vibrations. A set of identical discrete resonators with mass m and stiffness k are connected to each plate in a hexagonal lattice configuration. The resonators are located at the nodes of the hexagons. Let $\boldsymbol{r}_{\alpha\beta}$ indicate the position vectors of these resonators in each plate, with the index β taking values in $\{t, b\}$ indicating the top and bottom plate, and α is an integer that labels the resonators in each plate. Fig. 2b displays a schematic of the top plate with resonators. The bottom plate is rotated at an angle $\phi = 21.78°$ with respect to the center of a hexagon so that the resonator locations in the two plates resemble the moiré lattice as shown in Fig. 2a. Note that the edges of the hexagonal lattice in Fig. 2(a,b) do not have any physical meaning and are shown for clarity. The unit cell of the resulting lattice is indicated by dashed at the bottom left corner in Fig. 2a, along with its expanded view in the inset. Similar to the hexagonal lattice, the lattice vectors of the moiré lattice are also at 60° to each other. As discussed above, it has 14 nodes in each layer with 2 nodal locations where the top and bottom layers coincide, as indicated by the green circles in the inset. The two plates are coupled by inter-layer springs of stiffness k_{in} at these coinciding locations. Fig. 2c displays a schematic of the fully assembled bilayered structure.

As noted earlier, each layer and thus the infinite lattice has 6-fold rotation symmetry about an axis through the unit cell center. In addition, the lattice also has a 2-fold rotation symmetry about both the short and long in-plane diagonals, as indicated by the dashed lines in Fig. 2a. Indeed, when the lattice is rotated by 180° about a diagonal, the top plate resonators go to the bottom plate resonators' locations. The resulting structure is thus identical to that prior to rotation. Note that this operation is not equivalent to simply interchanging the top and bottom layers, as the latter will result in a different lattice.

Let us now present the governing equations for elastic waves in this bilayered structure. We assume that the out-of-plane modes are decoupled from the in-plane longitudinal and shear modes. In addition, we assume each resonator has one degree of freedom and can move out-of-plane. The out-of-plane displacement of a resonator located at $\boldsymbol{r}_{\alpha\beta}$ and the mid-plane section of plate β are denoted by $w_{\alpha\beta}$ and w_β, respectively. The dynamics of these thin plates are modeled using the Kirchhoff–Love theory. The equation of motion of the combined structure having N moiré unit cells is given by [17,43]

$$D\nabla^4 w_\beta + \rho h \ddot{w}_\beta = -\sum_{\alpha=1}^{14N} k(w_\beta - w_{\alpha\beta})\delta(\boldsymbol{x} - \boldsymbol{r}_{\alpha\beta}) - \sum_{\alpha=1}^{2N} k_{in}(w_\beta - w_{\beta'})\delta(\boldsymbol{x} - \boldsymbol{r}_{\alpha\beta}), \tag{7a}$$

$$m\ddot{w}_{\alpha\beta} = -k(w_{\alpha\beta} - w_\beta(\boldsymbol{r}_{\alpha\beta})). \tag{7b}$$

Here $\boldsymbol{x} = (x, y)$, which denotes the position vector of a point in the plane of the plates, and the gradient operator ∇ in Eq. (7a) is with respect to $\boldsymbol{x}$. The first term on the right-hand side of Eq. (7a) accounts for force due to the resonators, while the last term is for the interaction between the two plates. Subscript (β, β') in this last term takes values $\{t, b\}$ and $\{b, t\}$ for the top and bottom plates, respectively. The plate bending stiffness is $D = Eh^3/12(1 - \nu^2)$, with thickness h, Young's modulus E, Poisson's ratio ν and its density is ρ. For N moiré unit cells, the number of resonators in each plate and the number of inter-layer springs are $14N$ and $2N$, respectively. The following dimension and properties are chosen for our numerical calculations: unit cell length $a = 26.5$ mm, $m = 10^{-3}$ kg, $k = 10$ kN/m, $k_{in} = 2$ kN/m, $h = 0.1$ mm, $E = 70$ GPa, $\nu = 0.33$, $\rho = 2700$ kg/m^3. The material properties correspond to aluminum as the plate material.

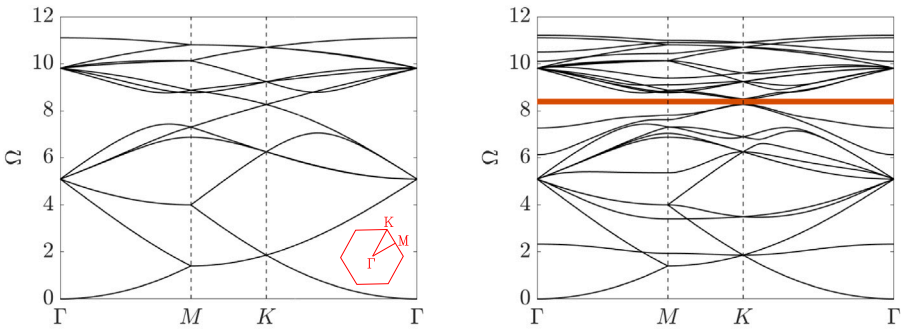

(a) $k_{in} = 0$ (b) $k_{in} \neq 0$

Fig. 3. Dispersion diagram of the unit cell along the IBZ boundary (a) without inter-layer springs ($k_{in} = 0$) and (b) with inter-layer springs ($k_{in} \neq 0$). The shaded band in (b) indicates a bandgap opening at the K-point.

3. Unit cell analysis

Having introduced the lattice description and presented the governing equations, we now do a dispersion analysis over its unit cell using the plane wave expansion method. We apply the approach followed in prior works on elastic plates with square and hexagonal array of resonators [17,44,45]. Then the topological properties of the dispersion bands are determined by computing the fractional corner mode Q, which is the elastic analogue of the fractional charge in electronic crystals [22]. This quantity is used to predict the existence of localized modes at the corners of a finite moiré lattice structure.

3.1. Dispersion analysis

We use Floquet–Bloch theory with the plane wave expansion method to determine waves propagating through the bilayered lattice. For a plane wave propagating with frequency ω and wave vector $\boldsymbol{\kappa}$, the displacement field in the plate may be expressed as

$$w_\beta(\boldsymbol{x}, t) = e^{i(\omega t + \boldsymbol{\kappa}\cdot\boldsymbol{x})} W_\beta(\boldsymbol{x}). \tag{8}$$

where $W_\beta(\boldsymbol{x})$ is a periodic function with periodicity of the moiré unit cell. This periodic function can be expressed using a Fourier series as $\sum_{l_1}\sum_{l_2} W_{l_1 l_2 \beta} e^{i(l_1 \boldsymbol{g_1}\cdot\boldsymbol{x} + l_2 \boldsymbol{g_2}\cdot\boldsymbol{x})}$, with $\boldsymbol{g_1}, \boldsymbol{g_2}$ being the reciprocal lattice vectors of the moiré lattice. They satisfy $\boldsymbol{g_i}\cdot\boldsymbol{a_j} = 2\pi\delta_{ij}$ and are given by $\boldsymbol{g_1} = 2\pi(1/a, -1/\sqrt{3}a)$ and $\boldsymbol{g_2} = 2\pi(0, 2/\sqrt{3}a)$. The summation indices run over all integers, but for computation purposes, we truncate the summations at T terms and use the approximation

$$w_\beta(\boldsymbol{x}, t) = e^{i(\omega t + \boldsymbol{\kappa}\cdot\boldsymbol{x})} \sum_{l_1, l_2 = -T}^{T} e^{i(l_1 \boldsymbol{g_1} + l_2 \boldsymbol{g_2})\cdot\boldsymbol{x}} W_{l_1 l_2 \beta}. \tag{9}$$

Here, $W_{l_1 l_2 \beta}$ denotes the plane wave coefficient subscripted by integers l_1, l_2 and finite number $(2T+1)^2$ of terms are considered. The resonator displacement can be expressed as

$$w_{\alpha\beta}(t) = e^{i(\omega t + \boldsymbol{\kappa}\cdot\boldsymbol{r}_{\alpha\beta})} W_{\bar{\alpha}\beta}. \tag{10}$$

Here the index $\bar{\alpha}$ takes values in $\{1, 2, \ldots, 14\}$ and labels the resonators in a reference unit cell, while the index α is an integer that labels resonators in an arbitrary unit cell in the lattice.

Let us derive the discrete form of the governing equations over the unit cell. Substituting the plate and resonator displacements into Eq. (7a), multiplying by $e^{-i(\boldsymbol{k}+\boldsymbol{g}')\cdot\boldsymbol{x}}$ and integrating over the unit cell gives an equation for each $W_{l_1 l_2 \beta}$. Similarly, substituting the displacements into Eq. (7b) gives an equation for each $W_{\bar{\alpha}\beta}$. The detailed derivations are presented in Appendix A.1. The resulting discretized governing equations are

$$\begin{aligned}\omega^2 W_{l_1' l_2' \beta} = {} & \frac{D}{\rho A h}|\boldsymbol{\kappa} + \boldsymbol{g}'|^4 W_{l_1' l_2' \beta} + \frac{k}{\rho A h}\sum_{\alpha=1}^{14} e^{-i\boldsymbol{g}'\cdot\boldsymbol{r}_{\alpha\beta}}\left(\sum_{l_1, l_2 = -T}^{T} e^{i\boldsymbol{g}\cdot\boldsymbol{r}_{\alpha\beta}} W_{l_1 l_2 \beta} - W_{\bar{\alpha}\beta}\right) \\ & + \frac{k_{in}}{\rho A h}\sum_{\alpha=1}^{2} e^{-i\boldsymbol{g}'\cdot\boldsymbol{r}_{\alpha\beta}}\left(\sum_{l_1, l_2 = -T}^{T} e^{i\boldsymbol{g}\cdot\boldsymbol{r}_{\alpha\beta}}(W_{l_1 l_2 \beta} - W_{l_1 l_2 \beta'})\right),\end{aligned} \tag{11a}$$

$$\omega^2 W_{\bar{\alpha}\beta} = -\frac{k}{m}\sum_{l_1, l_2 = -T}^{T} e^{i\boldsymbol{g}\cdot\boldsymbol{r}_{\alpha\beta}} W_{l_1 l_2 \beta} + \frac{k}{m} W_{\bar{\alpha}\beta}. \tag{11b}$$

Here $\boldsymbol{g} = l_1\boldsymbol{g_1} + l_2\boldsymbol{g_2}$, $\boldsymbol{g}' = l_1'\boldsymbol{g_1} + l_2'\boldsymbol{g_2}$ and $A = \sqrt{3}a^2/2$ is the unit cell area. Eqs. (11a) and (11b) together constitute an eigenvalue problem and its solution gives the dispersion relation of the unit cell yielding the frequencies ω at specific wave number, $\boldsymbol{\kappa}$. We

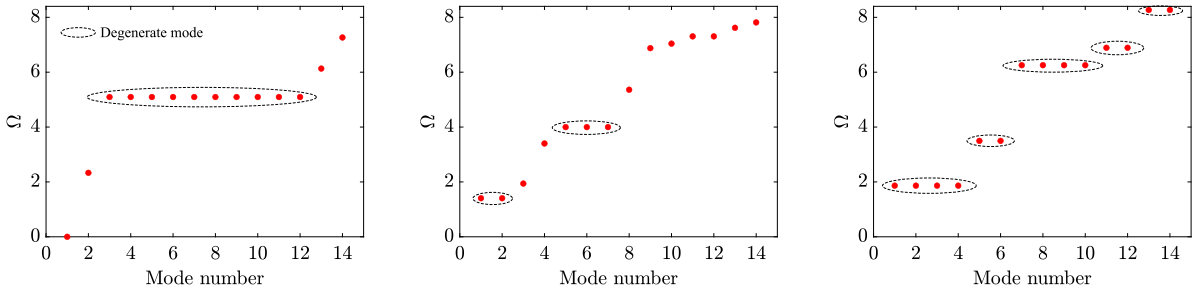

Fig. 4. Frequencies of first 14 bands below the bandgap at various high symmetry points of the irreducible Brillouin zone. There are a number of degenerate modes, which require a Gram Schmidt procedure to determine their rotational eigenvalue λ_ρ.

present results for calculations with $T = 10$. Increasing T beyond this value did not result in a noticeable change in the results. Finally, the frequency ω is expressed in non-dimensional form using the normalization $\Omega = \sqrt{\rho a^4 h/D}\omega$.

As discussed earlier in Section 2.2, the infinite lattice has 6-fold rotation symmetry about an out of plane axis through the unit cell center and 2-fold rotation symmetry about its in-plane diagonals. Thus its Brillouin zone is a hexagon and its irreducible Brillouin zone (IBZ) comprises of a triangle whose corners are the high symmetry points $\Gamma = (0,0)$, $M = (\pi/a, \pi/\sqrt{3}a)$ and $K = (2\pi/3a, 2\pi/\sqrt{3}a)$. Here, we examine the dispersion surfaces along the boundary of the IBZ.

Fig. 3 displays the dispersion diagram of a unit cell for points along Γ-M-K-Γ in the IBZ for two cases: (a) the plates are uncoupled, $k_{in} = 0$ and (b) coupled by inter-layer springs, $k_{in} \neq 0$. The inset in (a) has a schematic of the Brillouin zone, IBZ, along with the high symmetry points. Since the spectrum of ∇^4 operator in Eq. (7a) is unbounded, the exact solution has an infinite number of frequencies at each wave vector. There is a huge bandgap above the first 28 dispersion branches in both cases, and we restrict attention to these branches only. For the uncoupled plate case, the dispersion diagram in Fig. 3(a) has a Dirac cone at K point, consistent with a Dirac cone that arises in a hexagonal lattice. A bandgap opens at that K point when inter-layer springs are added, indicated by the shaded rectangle in Fig. 3(b). In addition, two branches become isolated from the remainder of the dispersion curves, consistent with other studies which find isolated flat bands at much smaller moiré angles [16].

3.2. Localized mode prediction by computing fractional corner mode Q

We use the dispersion analysis to determine if a finite moiré structure has localized modes at its boundary. The bulk edge correspondence principle relates the symmetry and topological properties of the Bloch modes in an infinite lattice to the modes localized on the boundaries of a finite lattice [21,46]. The presence of localized modes can be predicted by computing appropriate topological invariants. Here, we will determine the elastic analog of the fractional corner charge Q, which has been introduced to predict and demonstrate localized modes in electronic and photonic media [21,22,47].

The fractional corner mode Q is a topological invariant determining the existence of higher order topological mode in the bandgap. This quantity measures the change in rotational symmetry of the Bloch modes as we traverse the dispersion surface. It is expressed in terms of the number of specific rotational symmetry eigenvalues of the Bloch modes at the high symmetry points. All the dispersion branches below the bandgap are considered to compute Q. There are 14 bands below the band gap shown in Fig. 3(b) for the moiré lattice. Fig. 4 displays the distribution of these 14 frequencies at the various high symmetry points. We note that there are several degenerate sets of frequencies.

Before computing Q, let us discuss how a mode shape at the high symmetry points transforms as the lattice is rotated by an angle about the center of a unit cell. First, let us consider the high symmetry point K and the rotation angle is $2\pi/3$. Under this rotation, the lattice geometry looks identical to that prior to rotation. Let $\boldsymbol{R}(\theta)$ the rotation matrix given by

$$\boldsymbol{R}(\theta) = \begin{pmatrix} \cos\theta & -\sin\theta \\ \sin\theta & \cos\theta \end{pmatrix},$$

and let $\boldsymbol{R}_1 = \boldsymbol{R}(2\pi/3)$. Recall that the bilayered plate has 6-fold rotation symmetry about a unit cell center and thus remains identical when rotated by θ. Let us indicate a plane wave with wave vector $\boldsymbol{\kappa}$ by $w_\beta(\boldsymbol{x}, \boldsymbol{\kappa})$. It is also a function of t and ω, these are not indicated for brevity. Thus for every plane wave $w_\beta(\boldsymbol{x}, \boldsymbol{\kappa})$, there is a corresponding plane wave with wave vector $\boldsymbol{R\kappa}$, whose mode shape is $w_\beta(\boldsymbol{Rx}, \boldsymbol{R\kappa})$. This condition leads to the relation

$$w_\beta(\boldsymbol{x}, \boldsymbol{\kappa}) = w_\beta\left(\boldsymbol{R}_1\boldsymbol{x}, \boldsymbol{R}_1\boldsymbol{\kappa}\right) = w_\beta\left(\boldsymbol{R}_1\boldsymbol{x}, \boldsymbol{\kappa} - \boldsymbol{g_1} - \boldsymbol{g_2}\right). \tag{12}$$

The second equality in the above equation follows by observing that the wave vector at K satisfies $\boldsymbol{R}_1\boldsymbol{\kappa} = \boldsymbol{\kappa} - (\boldsymbol{g_1} + \boldsymbol{g_2})$, i.e., it translates by $-(\boldsymbol{g_1} + \boldsymbol{g_2})$ when rotated by $\theta = 2\pi/3$. The Bloch mode shapes at wave vector $\boldsymbol{\kappa} - \boldsymbol{g_1} - \boldsymbol{g_2}$ are identical to that at $\boldsymbol{\kappa}$, as the term $e^{-i(\boldsymbol{g_1}+\boldsymbol{g_2})\cdot\boldsymbol{x}}$ relating them in Eq. (8) is a periodic function [48]. Each set of corresponding Bloch modes at these two wave vectors may differ by a phase factor λ as we continuously traverse the reciprocal lattice [49]. Hence, we have $w_\beta(\boldsymbol{x}, \boldsymbol{\kappa} - \boldsymbol{g_1} - \boldsymbol{g_2}) = \lambda w_\beta(\boldsymbol{x}, \boldsymbol{\kappa})$.

Substituting this relation for a point $\boldsymbol{R_1 x}$ into the right side of Eq. (12), we see that the displacements at $\boldsymbol{x}$ and $\boldsymbol{R}_1\boldsymbol{x}$ in a Bloch mode shape at the K point are related by

$$w_\beta(\boldsymbol{x},\boldsymbol{\kappa}) = \lambda w_\beta(\boldsymbol{R}_1\boldsymbol{x},\boldsymbol{\kappa}). \tag{13}$$

Applying Eq. (13) successively three times, we get the relation $w_\beta(\boldsymbol{x},\boldsymbol{\kappa}) = \lambda^3 w_\beta(\boldsymbol{R}_1^3\boldsymbol{x},\boldsymbol{\kappa})$. Noting that $\boldsymbol{R}_1^3$ is the identity matrix, we have $\lambda^3 = 1$. Its solutions are

$$\lambda_p = e^{i2\pi(p-1)/3},\ p \in \{1,2,3\}.$$

Thus each mode shape $w_\beta(\boldsymbol{x})$ at the high symmetry point K satisfies Eq. (13) for a specific value of λ_p. This λ_p can thus be viewed as the eigenvalue of the rotational symmetry operator $\boldsymbol{R}_1$ for the mode shape.

Let us now describe the procedure to find the rotational eigenvalue λ_p for each Bloch mode at the K point. We project a mode shape into the subspace where a function $u(\boldsymbol{x})$ satisfies $u(\boldsymbol{R}_1\boldsymbol{x}) = \lambda_p u(\boldsymbol{x})$. The projected mode is given by

$$w_\beta^p(\boldsymbol{x}) = \frac{1}{3}\left(w_\beta(\boldsymbol{x}) + \lambda_p^{-1} w_\beta(\boldsymbol{R_1 x}) + \lambda_p^{-2} w_\beta(\boldsymbol{R_1^2 x})\right),\ p \in \{1,2,3\}.$$

By direct substitution, we can verify that any mode shape is decomposed into three parts w_β^p, that satisfy $w_\beta(\boldsymbol{x}) = w_\beta^1(\boldsymbol{x}) + w_\beta^2(\boldsymbol{x}) + w_\beta^3(\boldsymbol{x})$. If a mode shape has rotational eigenvalue $\lambda_q, q \in \{1,2,3\}$, then the component w_β^q is non-zero, while the other two projected components are zero. For example, if a mode satisfies $w_\beta(\boldsymbol{x}) = \lambda_1 w_\beta(\boldsymbol{R_1 x})$, then $w_\beta^1(\boldsymbol{x}) = w_\beta(\boldsymbol{x})$ and $w_\beta^2(\boldsymbol{x}) = w_\beta^3(\boldsymbol{x}) = 0$. Thus examining the norms or magnitudes of $w_\beta^p(\boldsymbol{x})$ suffices to identify λ_p for a non-degenerate mode. Next, let us discuss how to deal with a set of modes with degenerate frequencies. Here $w_\beta^p(\boldsymbol{x})$, determined by the above equation, can all be non-zero, as $w_\beta(\boldsymbol{x})$ may be a linear combination of mode shapes with distinct λ_p. To resolve this, we first determine $w_\beta^p(\boldsymbol{x})$ for all the mode shapes, say n_d, at a particular degenerate frequency. Then, for each p, a Gram–Schmidt procedure is done on the n_d projected modes $w_\beta^p(\boldsymbol{x})$. The number of orthogonal modes with non-zero norm gives the number of independent $w_\beta^p(\boldsymbol{x})$, which is equal to the number of modes with rotational eigenvalue λ_p in this set of n_d modes.

We follow a similar approach to determine the rotational eigenvalues at the other high symmetry points M and Γ. The wave vector at M satisfies $\boldsymbol{R}(\pi)\boldsymbol{\kappa} = \boldsymbol{\kappa} - \boldsymbol{g_1} - \boldsymbol{g_2}$. Again, we note that the lattice looks identical prior to and after rotation by $\theta = \pi$. Using the same steps as for the K point, the corresponding λ_p are

$$\lambda_p = e^{i2\pi(p-1)/2} = (-1)^{p-1},\ p \in \{1,2\},$$

and the projected modes are

$$w_\beta^p(\boldsymbol{x}) = \frac{1}{2}\left(w_\beta(\boldsymbol{x}) + (-1)^{p-1} w_\beta(\boldsymbol{R}(\pi)\boldsymbol{x})\right),\ p \in \{1,2\}.$$

Examining the norms of w_β^p or using a Gram Schmidt procedure for the sets with degenerate frequencies allows us to determine λ_p for each mode. The wave vector at Γ point satisfies both $\boldsymbol{R}(2\pi/3)\boldsymbol{\kappa} = \boldsymbol{\kappa}$ and $\boldsymbol{R}(\pi)\boldsymbol{\kappa} = \boldsymbol{\kappa}$. For each mode at Γ, we can thus determine the rotational eigenvalues λ_p for rotations by $2\pi/3$ and π. The mode shapes w_β^p corresponding to each λ_p for all the high symmetry points are presented in Appendix B, see Figs. 9–12.

The fractional corner mode Q, analogous to its electronic counterpart, is given by [42]

$$Q = \frac{[M_1^{(2)}]}{4} + \frac{[K_1^{(3)}]}{6} \mod 1. \tag{14}$$

Here, $[M_1^{(2)}]$ is the difference between the number of modes at M and Γ points that have $\lambda_p = 1$ under rotation by $\theta = \pi$. Similarly, $[K_1^{(3)}]$ denotes the difference between the number of mode shapes at K and Γ points with $\lambda_p = 1$ under rotation by $\theta = 2\pi/3$. Counting the number of mode shapes with $p = 1$ at the high symmetry points below the bandgap, we have from Eq. (14)

$$Q = \frac{(6-8)}{4} + \frac{(4-6)}{6} = \frac{-5}{6} = \frac{1}{6} \mod 1. \tag{15}$$

A non-zero value of Q in Eq. (15) confirms the non-trivial topological nature of the bandgap, which in turn, implies the existence of corner localized modes in a finite structure.

We apply the framework established by Hughes and coworkers [22] in the context of electronic waves and charges to predict the location of localized modes. This framework allows us to express the stiffness matrix of any C_6 symmetric structure as a direct sum of copies of the stiffness matrices of primitive generator lattices. The topological invariants, like Q, are a sum of the corresponding Q values of these primitive generators. We consider two primitive generators: h_{4b}, h_{3c} that have nontrivial topological properties. Here, a lattice with notation h_{mW} has m bands below the bandgap and a Wannier center at location W [22]. The lattice schematics, unit cell and dispersion diagrams for these two lattices are presented in Appendix C.

We computed the fractional corner modes for these primitive generator lattices by considering both 6-fold and 3-fold rotation symmetry. The values are $Q_6 = 2/3,\ Q_3 = 1/3$ for the $h4b$ lattice and $Q_6 = 1/2,\ Q_3 = 0$ for the $h3c$ lattice. Here, the subscripts of Q indicate the rotation symmetry of the finite structure. Thus Q_6 and Q_3 determine localized modes at 120° and 60° corners, respectively. These values show that the $h4b$ lattice has a localized mode at 60° corner, while both lattices have at 120° corner. Noting that Q of the moiré lattice may be expressed as $Q = 1/6 = 2/3 + 1/2 \pmod 1$, we infer that the moiré lattice is equivalent to stacking a copy of each of these two primitive generators, along with copies of a lattice (t) that has trivial topological properties.

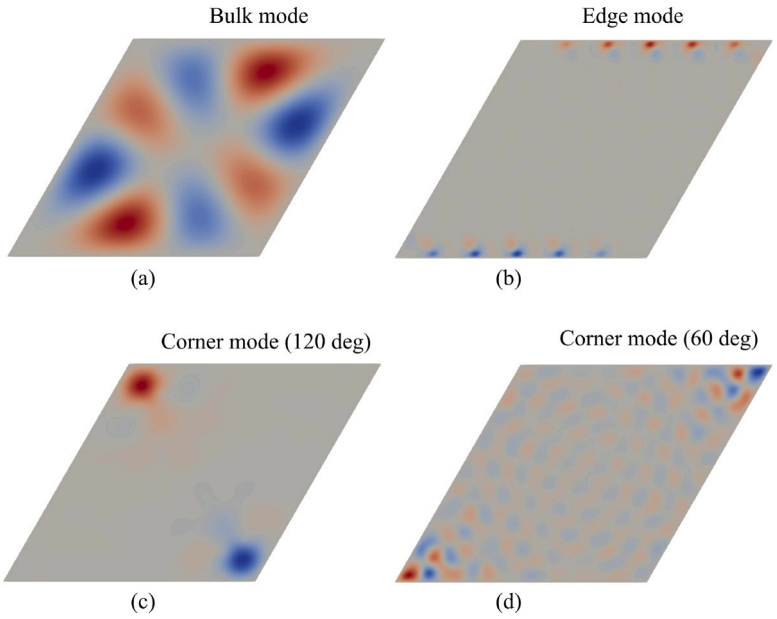

Fig. 5. Mode shapes of a finite plate with simply-supported boundary conditions. Displacement contours of top plate for (a) a typical bulk mode ($\Omega = 0.70$), (b) an edge mode ($\Omega = 13.71$), corner modes at (c) 120° corner ($\Omega = 2.34$) and (d) 60° corner ($\Omega = 8.19$).

In other words, the stiffness matrix of the moiré lattice, expressed in the basis of the first 28 dispersion bands, is equivalent to the direct sum $h4b \oplus h3c \oplus 7t$. This direct sum, along with the Q values of the primitive generators, indicates the existence of corner localized modes at both 120° and 60° corners in our moiré structure. Indeed, the latter case of 60° corner localized mode is inferred by noting that the Q_3 value of our moiré lattice is $1/3 + 0 = 1/3$.

4. Numerical results of finite plate

In this section, the predictions of corner localized modes in Section 3.2 are verified by determining the mode shapes and frequency response under external excitation on a finite plate. We show that these localized modes are excited even when an external force is applied far from the corner.

4.1. Bulk and localized mode shapes

We consider a finite plate of $n_1 \times n_2 = 6 \times 6$ moiré unit cells along $\boldsymbol{a_1}$, $\boldsymbol{a_2}$ directions. The sides of the plate are of lengths L_1 and L_2, both equal to $6a$. The four sides of the plate are simply supported, implying zero displacement and zero bending moment about an axis along the boundary. At each boundary point, these conditions may be expressed as [50]

$$w_\beta = 0, \quad M_\eta = \frac{\partial^2 w_\beta}{\partial \eta^2} + \nu \frac{\partial^2 w_\beta}{\partial \tau^2} = 0,$$

with η and τ being coordinates normal to and along the boundary.

We introduce and work with a coordinate system whose axes (x_1, x_2) are aligned with the lattice vectors of the moiré lattice. The boundary conditions and solution basis functions are conveniently expressed in this coordinate system. To determine the governing equations in this coordinate system, let us determine its relation with the Cartesian coordinate system having axes (x, y). Let us consider an arbitrary point with position vector $\boldsymbol{x}$ in the two coordinate systems. It is given by $\boldsymbol{x} = x\boldsymbol{e_x} + y\boldsymbol{e_y} = x_1\boldsymbol{e_1} + x_2\boldsymbol{e_2}$, with $(\boldsymbol{e_x}, \boldsymbol{e_y})$ and $(\boldsymbol{e_1}, \boldsymbol{e_2})$ being unit vectors in the two coordinate systems. Taking dot products with $\boldsymbol{e_x}$ and $\boldsymbol{e_y}$ gives the relations $x = x_1 + x_2/2$ and $y = \sqrt{3}x_2/2$. They can be inverted to get $x_1 = x - y/\sqrt{3}$ and $x_2 = 2y/\sqrt{3}$.

The boundary conditions in the new coordinate system become

$$w_\beta(x_1 = 0, x_2) = w_\beta(x_1 = L_1, x_2) = w_\beta(x_1, x_2 = 0) = w_\beta(x_1, x_2 = L_2) = 0,$$
$$\left.\frac{\partial^2 w_\beta}{\partial x_1^2}\right|_{(x_1=0)} = \left.\frac{\partial^2 w_\beta}{\partial x_1^2}\right|_{(x_1=L_1)} = \left.\frac{\partial^2 w_\beta}{\partial x_2^2}\right|_{(x_2=0)} = \left.\frac{\partial^2 w_\beta}{\partial x_2^2}\right|_{(x_2=L_2)} = 0.$$

The plate displacement, $w_\beta(\boldsymbol{x}, t)$ is approximated using a set of harmonic basis functions as

$$w_\beta(\boldsymbol{x}, t) = e^{i\omega t} \sum_{p=1}^{N_1} \sum_{q=1}^{N_2} \sin\frac{p\pi x_1}{L_1} \sin\frac{q\pi x_2}{L_2} W_{pq\beta}. \tag{16}$$

Table 1
Symmetry property of the modes in Fig. 5 under 180° rotation about its short and long diagonals.

–	Bulk	Edge	Corner(120°)	Corner(60°)
Short diagonal	Odd	Even	Odd	Odd
Long diagonal	Odd	Odd	Even	Even

Note that these basis functions satisfy all the above boundary conditions. Similarly, the resonator displacements, $w_{\alpha\beta}(t)$ can be written as

$$w_{\alpha\beta}(t) = e^{i\omega t} W_{\alpha\beta}, \tag{17}$$

with the index α ranging from 1 to $14 \times n_1 \times n_2$.

Let us now derive the discrete approximations of the governing equations for vibration at frequency ω. Substituting the above displacements into Eq. (7a), multiplying by $\sin(p'\pi x_1/L_1)\sin(q'\pi x_2/L_2)$ and integrating over the finite plate leads to an equation for each basis function. Similarly, substituting the displacements into Eq. (7b) gives an equation for each resonator displacement amplitude $W_{\alpha\beta}$. The detailed derivations are presented in Appendix A.2. The discretized governing equations thus obtained are

$$\begin{aligned}
\omega^2 W_{p'q'\beta} = {} & \frac{16\pi^4 D}{9\rho h L_1^4 L_2^4}\left(p'^4 L_2^4 + 3p'^2 q'^2 L_1^2 L_2^2 + q'^4 L_1^4\right) W_{p'q'\beta} \\
& + \frac{32p'q'D}{9\rho h}\sum_{\substack{p=1\\p\neq p'}}^{N_1}\sum_{\substack{q=1\\q\neq q'}}^{N_2}\frac{pq}{L_1 L_2}\left\{\left(\frac{p\pi}{L_1}\right)^2 + \left(\frac{q\pi}{L_2}\right)^2\right\}\left[\frac{(-1)^{p+p'}-1}{p^2-p'^2}\right]\left[\frac{(-1)^{q+q'}-1}{q^2-q'^2}\right] W_{pq\beta} \\
& + \frac{8k}{\sqrt{3}\rho h L_1 L_2}\sum_{\alpha=1}^{14n_1n_2}\sin\frac{p'\pi r_{\alpha\beta 1}}{L_1}\sin\frac{q'\pi r_{\alpha\beta 2}}{L_2}\left[\sum_{p=1}^{N_1}\sum_{q=1}^{N_2}\sin\frac{p\pi r_{\alpha\beta 1}}{L_1}\sin\frac{q\pi r_{\alpha\beta 2}}{L_2} W_{pq\beta} - W_{\alpha\beta}\right] \\
& + \frac{8k_{in}}{\sqrt{3}\rho h L_1 L_2}\sum_{\alpha=1}^{2n_1n_2}\sin\frac{p'\pi r_{\alpha 1}}{L_1}\sin\frac{q'\pi r_{\alpha 2}}{L_2}\left[\sum_{p=1}^{N_1}\sum_{q=1}^{N_2}\sin\frac{p\pi r_{\alpha 1}}{L_1}\sin\frac{q\pi r_{\alpha 2}}{L_2}\left(W_{pq\beta} - W_{pq\beta'}\right)\right],
\end{aligned} \tag{18a}$$

$$\omega^2 W_{\alpha\beta} = \frac{k}{m} W_{\alpha\beta} - \frac{k}{m}\sum_{p=1}^{N_1}\sum_{q=1}^{N_2}\sin\frac{p\pi r_{\alpha\beta 1}}{L_1}\sin\frac{q\pi r_{\alpha\beta 2}}{L_2} W_{pq\beta}. \tag{18b}$$

Here $\boldsymbol{r}_{\alpha\beta} = r_{\alpha\beta 1}\boldsymbol{e}_1 + r_{\alpha\beta 2}\boldsymbol{e}_2$ and $\boldsymbol{r}_{\alpha} = r_{\alpha 1}\boldsymbol{e}_1 + r_{\alpha 2}\boldsymbol{e}_2$ are the position vectors of resonators and inter-layer springs expressed in the (x_1, x_2) coordinate system. Here, Eqs. (18a) and (18b) together constitute an eigenvalue problem of the form $\omega^2\boldsymbol{v} = \boldsymbol{K}\boldsymbol{v}$, with $\boldsymbol{v} = [\boldsymbol{W}_{pqt}; \boldsymbol{W}_{pqb}; \boldsymbol{W}_{\alpha t}; \boldsymbol{W}_{\alpha b}]$ being the vector whose components are coefficients of basis functions for both the plate and resonator displacements. $\boldsymbol{K}$ is the stiffness matrix containing the right-hand side terms in Eqs. (18a) and (18b). The solution of the eigenvalue problem provides the mode shapes at the corresponding frequencies, ω. Each mode shape has 4 parts: displacement fields of the top and bottom plates w_β, and the vector of resonator displacements $W_{\alpha\beta}$ in each plate.

Let us remark on the relation between the displacement fields in the plates based on symmetry considerations. Note that the finite bilayer structure also has C_2 symmetry about each of its diagonals, similar to the infinite lattice (see Fig. 2a). The mode shapes of the finite plate are thus eigenvectors of this symmetry operator. Since the C_2 rotation operator has eigenvalues $\lambda = \pm 1$, each mode shape remains the same or changes sign under a rotation by π along a diagonal. We observe that this symmetry operation is equivalent to reflecting each plate in its plane about a diagonal, followed by interchanging the two plates. Thus, an equivalent way to express the above symmetry condition is the following: for each mode shape, if the top plate displacement field is reflected about a diagonal, it will be same ($\lambda = +1$) or negative ($\lambda = -1$) of the bottom plate displacement field. Note that the λ values can be distinct when reflected about the short and long diagonals for a mode shape.

The results are reported for calculations with $N_1 = N_2 = 50$ terms. We also did calculations with $N_1 = N_2 = 60$, and did not observe a noticeable difference in the mode shapes. Displacement contours at the top plate are illustrated in Fig. 5 for a few representative mode shapes. The bottom plate displacement field, top and bottom resonator displacements for these mode shapes are presented in Appendix D, see Figs. 14 and 15. We find that the resonator displacements are in phase with their plate displacements for all of these modes. As discussed above, a mode shape may change sign or remain unchanged under rotation by π about a diagonal. This relation may be determined by examining the displacement fields of top and bottom plates. They are tabulated below for each mode in Fig. 5 and for each diagonal rotation axis. The modes that remain identical and that change sign under rotation are labeled even and odd, respectively (see Table 1).

The edge localized mode in Fig. 5b has a counterpart at the same frequency, that is localized at the other edges. The mode shape of this counterpart is included in Appendix D. These edge modes lie in the bandgap above the first 28 dispersion branches. They do not have a topological origin and may become bulk modes when boundary conditions or material properties are varied. In contrast, the corner localized modes shown in Fig. 5(c–d) arise due to the symmetry and topological properties of dispersion bands. The mode localized at the 120° lies in the bulk band frequency, while the 60° corner localized mode lies in the bandgap. These localized modes verify the prediction of higher order topological mode at both corners as discussed in Section 3.2.

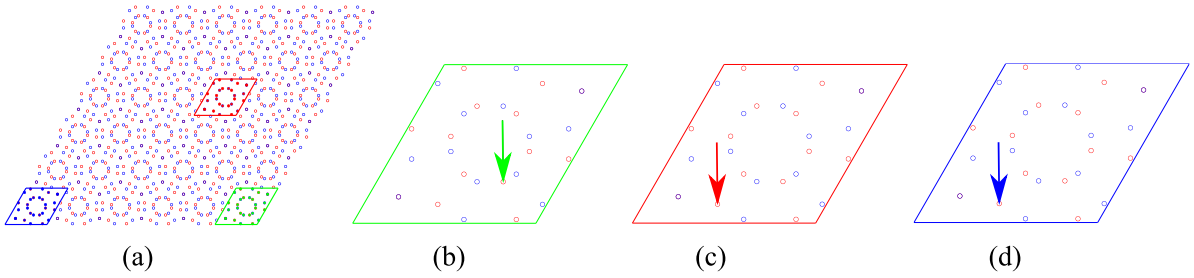

Fig. 6. Schematic of the finite lattice showing different excitation and response locations. (a) Responses are evaluated over the unit cell indicated by parallelogram at 120° corner, interior and 60° corner. Excitations are given at a resonator in the top plate indicated by arrow in (b) 120° corner, (c) interior and (d) 60° corner.

4.2. Frequency response under harmonic excitation

Finally, let us analyze the effect of these topological corner localized modes on the steady-state dynamic response under external excitation. To this end, we determine the frequency response by applying a harmonic force and measuring the steady state response at various locations (see Fig. 6) in the finite lattice. An excitation $fe^{i\omega t}$ is applied at one resonator in the top plate, indicated by an arrow in Fig. 6(b–d). We choose the excitation points at the 120° and 60° corners such that the resonators there have a higher magnitude in the respective mode shapes localized at those corners in Fig. 15(d,e). The excitation point for interior excitation in Fig. 6(c) is chosen arbitrarily, to be the same resonator in the unit cell in Fig. 6(d). The equations for solving the frequency response is $\omega^2\boldsymbol{v} - \boldsymbol{K}\boldsymbol{v} = \boldsymbol{f}$, where $\boldsymbol{f}$ is the external force vector. It takes 1 associated to the excitation point and rest values are 0. The considered frequency spacing in the calculation is $\Delta\omega = 1.0 \times 10^{-2}$ rad/s, or in non-dimensional units, $\Delta\Omega = 4.50 \times 10^{-5}$. For each case, responses are also observed at the 120° corner, interior and 60° corner region over a unit cell indicated by parallelogram in Fig. 6a. The response is computed using the expression

$$\frac{|u|}{f} = \sqrt{\sum_{\beta=\{t,b\}} \sum_{\alpha=1}^{14} \left| w_{\alpha\beta} \right|^2}. \tag{19}$$

To illustrate the effect of corner localized modes in Fig. 5(c–d) on the frequency response function of a finite plate, we excite it in a range of frequencies around these natural frequencies. Recall that the 120° and 60° corner localized mode frequencies are 2.34 and 8.19, respectively. At each frequency, we excite the lattice at 3 locations: at a 60° and a 120° corner, and in the interior, and determine the response of the unit cells at these locations using Eq. (19). These locations are indicated in Fig. 6.

Fig. 7(a–c) displays the frequency response near $\Omega = 2.34$, with each sub-figure for a different excitation location. For the 120° corner excitation, Fig. 7a displays the response at various locations in the finite plate indicated in Fig. 6a. The peak responses at all locations happen at frequency 2.34, as indicated by a "star" in the figure. The response of the 120° corner unit cell is higher than at other locations, since it is close to the excitation point. Similarly, Fig. 7(b–c) displays the response for excitations at the interior and 60° corner locations. Even when the excitation is far from the 120° corner, the peak response at the localized mode frequency is the highest at this corner. This peak response shows that the corner localized mode gets excited regardless of the excitation location in the plate. In contrast, away from the localized mode frequency, we note that the response is higher close to the excitation location. See for example, the response to 60° corner excitation in Fig. 7c. Fig. 7d displays the displacement contours of the top plate for an excitation $\Omega = 2.34$ at 120° corner, which is similar to the mode shape in Fig. 5c. The displacement contours for excitation at interior and 60° corner locations have similar profile, but with lower peak magnitudes of 7.96×10^3 and 4.95×10^1, respectively.

Similarly, Fig. 8(a–c) displays the frequency response around $\Omega = 8.19$ for various excitation locations. Again, the peak response happens at the localized mode frequency and the 60° corner has the highest displacement magnitude $|u|/f$, regardless of the excitation location. Fig. 8d illustrates the displacement contour of top plate for excitation at 60° corner, confirming that the steady-state response is localized at the 60° corner. The displacement contours for excitation at the 120° corner and interior have a similar profile, but with different maximum magnitudes of 9.87×10^3 and 2.66×10^3, respectively. These calculations verify the presence of corner localized modes at both corners of the finite moiré plates.

5. Conclusions

We investigated corner localized modes that arise due to higher order topology in moiré lattices of bilayer elastic plates. Each plate has a hexagonal array of resonators and one of the plates is rotated at an angle (21.78°) which results in a periodic moiré lattice with the smallest area. The resulting structure opens a band gap when inter-layer springs are added. The fractional corner mode Q is found to be 1/6 for dispersion bands below the bandgap. The non-zero value of Q indicates the non-trivial topological nature of the bandgap and predicts the existence of localized modes at all corners in the finite structure. Modal analysis on a finite plate showed the existence of these corner localized modes at both 60° and 120° corners. The first one lies in the bulk band frequency and the later one lies in the bandgap frequency. Finally, the frequency response under external excitation at various locations shows

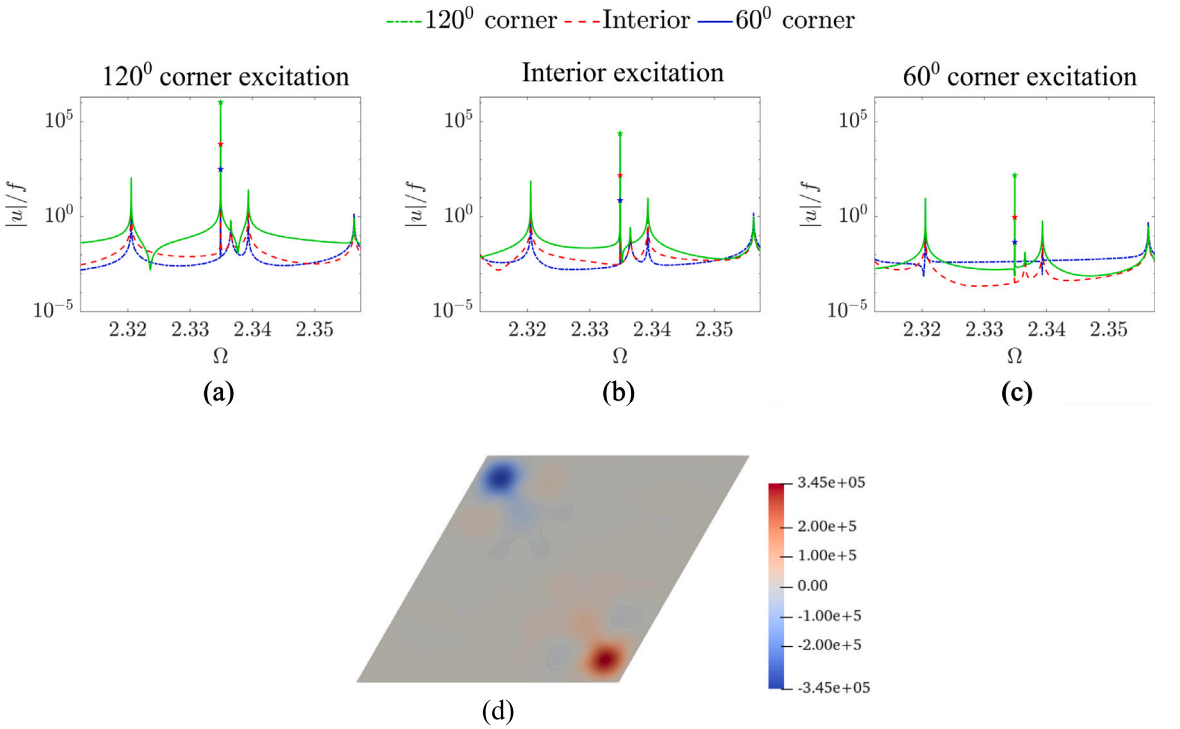

Fig. 7. Frequency response and displacement contour near the 120° corner localized frequency. Excitation is given at (a) 120° corner, (b) interior and (c) 60° corner and response are also shown at 120° corner, interior and 60° corner. (d) Top plate displacement contour for 120° corner excitation at frequency 2.34.

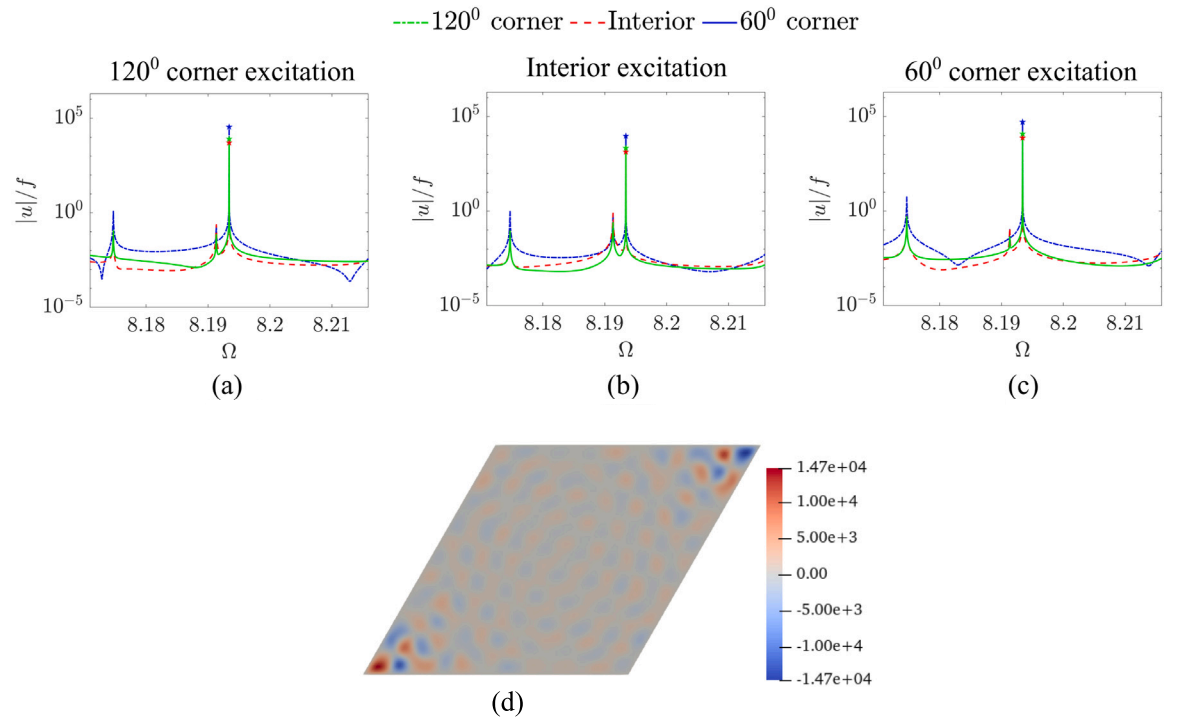

Fig. 8. Frequency response and displacement contour near the 60° corner localized frequency. Excitation is given at (a) 120° corner, (b) interior and (c) 60° corner and response are also shown at 120° corner, interior and 60° corner. (d) Top plate displacement contour for 60° corner excitation at frequency 8.19.

mode localization at these frequencies, consistent with the theoretical predictions. The considered continuous elastic moiré lattice structures open opportunities for seeking novel wave phenomena with potential applications in tunable energy localization, vibration isolation, and energy harvesting.

CRediT authorship contribution statement

Tamanna Akter Jui: Data curation, Formal analysis, Investigation, Methodology, Project administration, Resources, Software, Visualization, Writing – original draft. **Raj Kumar Pal:** Conceptualization, Formal analysis, Funding acquisition, Investigation, Methodology, Project administration, Supervision, Writing – review & editing.

Declaration of competing interest

The authors declare that they have no known competing financial interests or personal relationships that could have appeared to influence the work reported in this paper.

Data availability

Data will be made available on request.

Acknowledgment

This work was supported by the U.S. National Science Foundation under Award No. 2238072.

Appendix A. Derivation of discrete governing equations

The detailed derivation of the discrete form of the governing equations in terms of the Fourier coefficients $W_{l_1 l_2 \beta}$ are presented for dispersion analysis and $W_{pq\beta}$ for finite plate analysis.

A.1. Dispersion analysis

We start by substituting the displacements in Eqs. (9) and (10) into the governing equation for the plate (7a), which leads to

$$(D|\boldsymbol{\kappa}+\boldsymbol{g}|^4-\rho h\omega^2)\sum_{l_1,l_2=-T}^{T} e^{i(\boldsymbol{k}+\boldsymbol{g}).\boldsymbol{x}} W_{l_1 l_2 \beta} = -k\sum_{\alpha=1}^{14N}\left[\sum_{l_1,l_2=-T}^{T} e^{i(\boldsymbol{k}+\boldsymbol{g}).\boldsymbol{x}} W_{l_1 l_2 \beta} - e^{i\boldsymbol{\kappa}.\boldsymbol{r}_{\alpha\beta}} W_{\bar{\alpha}\beta}\right]\delta(\boldsymbol{x}-\boldsymbol{r}_{\alpha\beta}) - k_{in}\sum_{\alpha=1}^{2N}\left[\sum_{l_1,l_2=-T}^{T} e^{i(\boldsymbol{k}+\boldsymbol{g}).\boldsymbol{x}}(W_{l_1 l_2 \beta} - W_{l_1 l_2 \beta'})\right]\delta(\boldsymbol{x}-\boldsymbol{r}_{\alpha\beta}). \tag{20}$$

We work in the (x_1, x_2) coordinate system, whose unit vectors are aligned with the moiré lattice vectors $(\boldsymbol{a_1}, \boldsymbol{a_2})$. It is related to the Cartesian coordinate system by $x_1 = x - y/\sqrt{3}$ and $x_2 = 2y/\sqrt{3}$. Multiplying by $e^{-i(\boldsymbol{k}+\boldsymbol{g}').\boldsymbol{x}}$, rearranging and integrating over a unit cell $\mathcal{D}$ gives

$$\begin{aligned}&\int_{\mathcal{D}}\sum_{l_1,l_2=-T}^{T}(D|\boldsymbol{\kappa}+\boldsymbol{g}|^4-\rho h\omega^2)e^{i(\boldsymbol{g}-\boldsymbol{g}').\boldsymbol{x}} W_{l_1 l_2 \beta}\, dx_1\wedge dx_2\\ &= -k\int_{\mathcal{D}}\sum_{\alpha=1}^{14N}\left[e^{-i\boldsymbol{g}'.\boldsymbol{x}}\left\{\sum_{l_1,l_2=-T}^{T} e^{i\boldsymbol{g}.\boldsymbol{x}} W_{l_1 l_2 \beta} - e^{i\boldsymbol{\kappa}.(\boldsymbol{r}_{\alpha\beta}-\boldsymbol{x})} W_{\bar{\alpha}\beta}\right\}\right]\delta(\boldsymbol{x}-\boldsymbol{r}_{\alpha\beta})\,dx_1\wedge dx_2\\ &\quad -k_{in}\int_{\mathcal{D}}\sum_{\alpha=1}^{2N}\left[e^{-i\boldsymbol{g}'.\boldsymbol{x}}\left\{\sum_{l_1,l_2=-T}^{T} e^{i\boldsymbol{g}.\boldsymbol{x}}(W_{l_1 l_2 \beta} - W_{l_1 l_2 \beta'})\right\}\right]\delta(\boldsymbol{x}-\boldsymbol{r}_{\alpha\beta})\,dx_1\wedge dx_2.\end{aligned} \tag{21}$$

Note that $dx_1 \wedge dx_2 = (\sqrt{3}/2)dx_1 dx_2$ is the area of an infinitesimal parallelogram in $\mathcal{D}$. Using orthogonality of the functions $e^{i\boldsymbol{g}.\boldsymbol{x}}$, we get

$$\begin{aligned}(D|\boldsymbol{\kappa}+\boldsymbol{g}'|^4-\rho h\omega^2)A W_{l_1' l_2' \beta} &= -k\sum_{\alpha=1}^{14N}\left[e^{-i\boldsymbol{g}'.\boldsymbol{r}_{\alpha\beta}}\left\{\sum_{l_1,l_2=-T}^{T} e^{i\boldsymbol{g}.\boldsymbol{r}_{\alpha\beta}} W_{l_1 l_2 \beta} - W_{\bar{\alpha}\beta}\right\}\right]\\ &\quad -k_{in}\sum_{\alpha=1}^{2N}\left[e^{-i\boldsymbol{g}'.\boldsymbol{r}_{\alpha\beta}}\left\{\sum_{l_1,l_2=-T}^{T} e^{i\boldsymbol{g}.\boldsymbol{r}_{\alpha\beta}}(W_{l_1 l_2 \beta} - W_{l_1 l_2 \beta'})\right\}\right].\end{aligned}$$

Here $A = \sqrt{3}a^2/2$ is the area of the moiré unit cell. Dividing both sides of the above equation by $\rho A h$ and rearranging gives Eq. (11a).

For the resonator, substituting the displacements in Eqs. (9) and (10) into their governing equations (7b) gives

$$-m\omega^2 e^{i\boldsymbol{\kappa}.\boldsymbol{r}_{\alpha\beta}} W_{\bar{\alpha}\beta} = -k e^{i\boldsymbol{\kappa}.\boldsymbol{r}_{\alpha\beta}} W_{\bar{\alpha}\beta} + k\sum_{l_1,l_2=-T}^{T} e^{i(\boldsymbol{k}+\boldsymbol{g}).\boldsymbol{r}_{\alpha\beta}} W_{l_1 l_2 \beta}.$$

Multiplying by $-e^{-i\boldsymbol{\kappa}.\boldsymbol{r}_{\alpha\beta}}/m$ gives Eq. (11b).

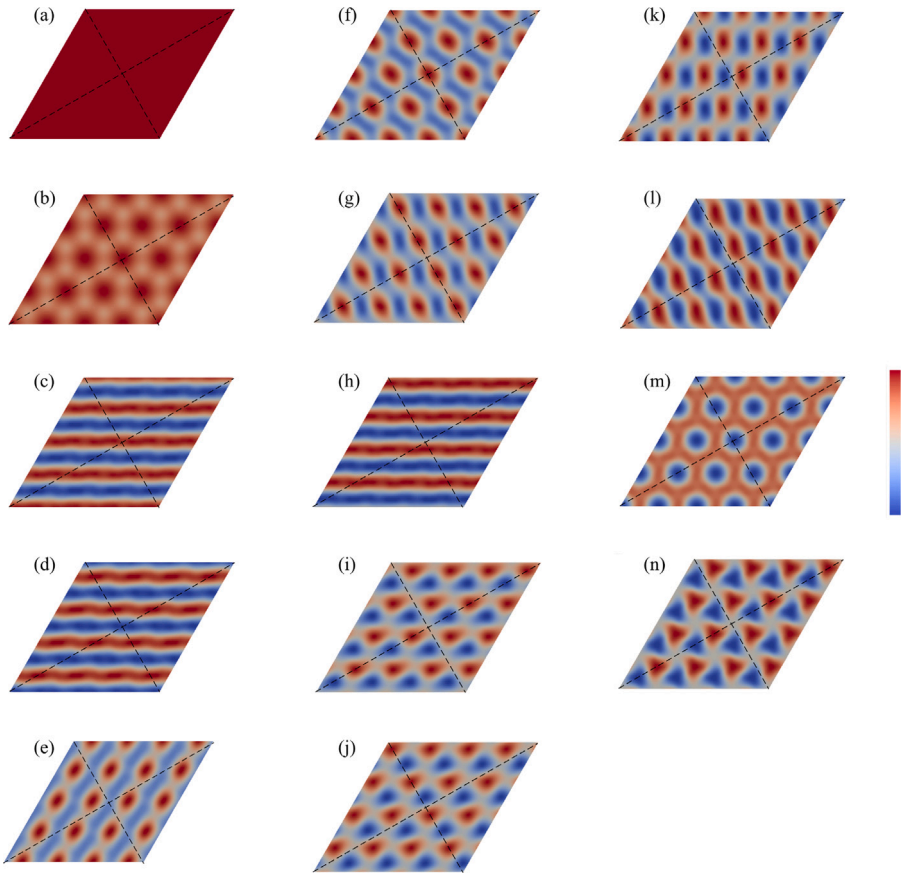

Fig. 9. Nonzero projected Bloch mode shapes under rotation by $\theta = \pi$ in the top plate at Γ point. Subfigures (a - n) correspond to modes (1–14). Modes having rotational eigenvalue $\lambda_1(p = 1)$: 1–7, 13 and $\lambda_2(p = 2)$: 8–12, 14. (4×4) unit cells are shown for clarity of rotational symmetry.

A.2. Derivation for finite plate frequencies and mode shapes

Let us derive the discrete equations that are used to determine the mode shapes and frequency response of a finite plate. Substituting the assumed displacement fields in Eqs. (16) and (17) into the governing equation Eq. (7a) for a plate gives

$$\begin{aligned}
&\sum_{p=1}^{N_1}\sum_{q=1}^{N_2}\left[\frac{1}{\sin^4\theta}\left(\frac{p\pi}{L_1}\right)^4+\frac{6}{\sin^2\theta\tan^2\theta}\left(\frac{p\pi}{L_1}\right)^2\left(\frac{q\pi}{L_2}\right)^2+\frac{1}{\sin^4\theta}\left(\frac{q\pi}{L_2}\right)^4+\frac{2}{\sin^2\theta}\left(\frac{p\pi}{L_1}\right)^2\left(\frac{q\pi}{L_2}\right)^2-\frac{\rho h\omega^2}{D}\right]\cdot\\
&W_{pq\beta}\sin\frac{p\pi x_1}{L_1}\sin\frac{q\pi x_2}{L_2}+\frac{4}{\tan\theta\sin^3\theta}\sum_{p=1}^{N_1}\sum_{q=1}^{N_2}\frac{p\pi}{L_1}\frac{q\pi}{L_2}\left\{\left(\frac{p\pi}{L1}\right)^2+\left(\frac{q\pi}{L2}\right)^2\right\}W_{pq\beta}\cos\frac{p\pi x_1}{L_1}\cos\frac{q\pi x_2}{L_2}\\
&=-\frac{k}{D}\sum_{\alpha=1}^{14N}\left[\sum_{p=1}^{N_1}\sum_{q=1}^{N_2}W_{pq\beta}\sin\frac{p\pi x_1}{L_1}\sin\frac{q\pi x_2}{L_2}-W_{\alpha\beta}\right]\delta(\boldsymbol{x}-\boldsymbol{r}_{\alpha\beta})\\
&\quad-\frac{k_{in}}{D}\sum_{\alpha=1}^{2N}\left[\sum_{p=1}^{N_1}\sum_{q=1}^{N_2}(W_{pq\beta}-W_{pq\beta'})\sin\frac{p\pi x_1}{L_1}\sin\frac{q\pi x_2}{L_2}\right]\delta(\boldsymbol{x}-\boldsymbol{r}_{\alpha\beta}).
\end{aligned}\tag{22}$$

Here, $\theta = 60°$ is the angle between the two lattice vectors. Multiplying by $\sin(p'\pi x_1/L_1)\sin(q'\pi x_2/L_2)$ and integrating over the lattice gives

$$\begin{aligned}
&\sum_{p=1}^{N_1}\sum_{q=1}^{N_2}\left[\frac{1}{\sin^4\theta}\left(\frac{p\pi}{L_1}\right)^4+\frac{6}{\sin^2\theta\tan^2\theta}\left(\frac{p\pi}{L_1}\right)^2\left(\frac{q\pi}{L_2}\right)^2+\frac{1}{\sin^4\theta}\left(\frac{q\pi}{L_2}\right)^4+\frac{2}{\sin^2\theta}\left(\frac{p\pi}{L_1}\right)^2\left(\frac{q\pi}{L_2}\right)^2-\frac{\rho h\omega^2}{D}\right]\sin\theta W_{pq\beta}\\
&\int_0^{L_1}\sin\frac{p\pi x_1}{L_1}\sin\frac{p'\pi x_1}{L_1}dx_1\int_0^{L_2}\sin\frac{q\pi x_2}{L_2}\sin\frac{q'\pi x_2}{L_2}dx_2+\frac{4}{\tan\theta\sin^3\theta}\sum_{p=1}^{N_1}\sum_{q=1}^{N_2}\frac{p\pi}{L_1}\frac{q\pi}{L_2}\left\{\left(\frac{p\pi}{L1}\right)^2+\left(\frac{q\pi}{L2}\right)^2\right\}\sin\theta W_{pq\beta}
\end{aligned}$$

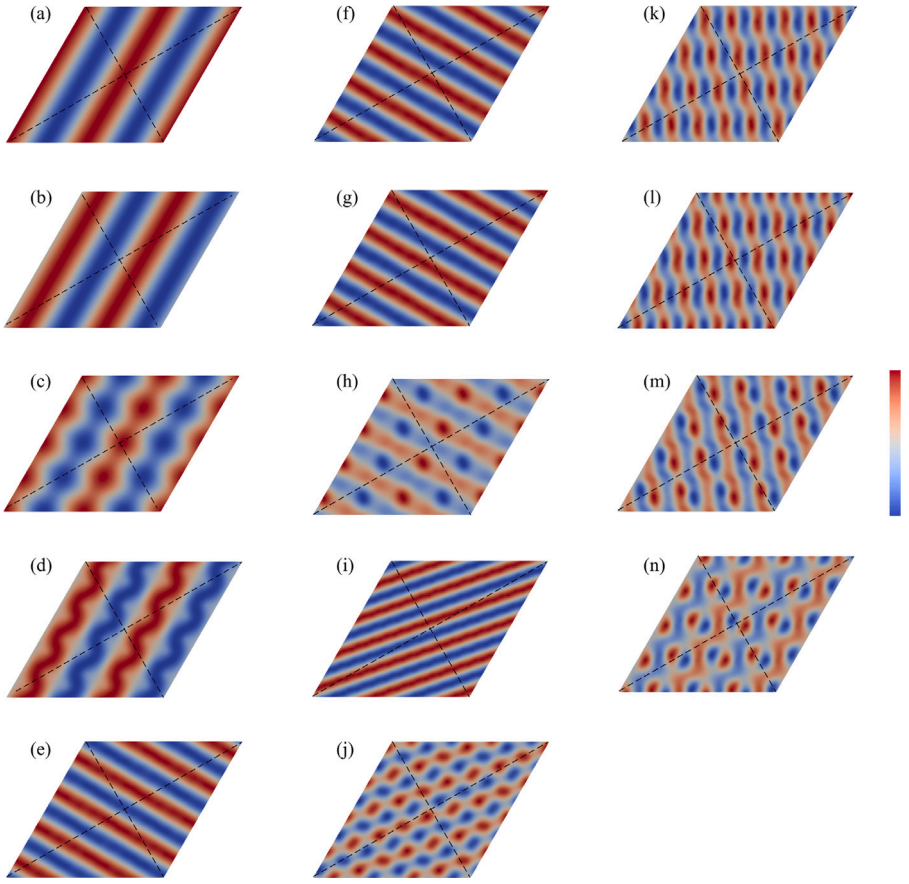

Fig. 10. Nonzero projected Bloch mode shapes under rotation by $\theta = \pi$ in the top plate at M point. Subfigures (a - n) correspond to modes (1–14). Modes having rotational eigenvalue $\lambda_1(p=1)$: 1, 3, 5, 8, 11, 13 and $\lambda_2(p=2)$: 2, 4, 6, 7, 9, 10, 12, 14. (4×4) unit cells are shown for clarity of rotational symmetry.

$$\int_0^{L_1} \cos\frac{p\pi x_1}{L_1}\sin\frac{p'\pi x_1}{L_1}dx_1\int_0^{L_2}\cos\frac{q\pi x_2}{L_2}\sin\frac{q'\pi x_2}{L_2}dx_2$$
$$= -\frac{k}{D}\sum_{\alpha=1}^{14N}\sin\frac{p'\pi x_1}{L_1}\sin\frac{q'\pi x_2}{L_2}\left[\sum_{p=1}^{N_1}\sum_{q=1}^{N_2}W_{pq\beta}\sin\frac{p\pi x_1}{L_1}\sin\frac{q\pi x_2}{L_2}-W_{\alpha\beta}\right]\iint\delta(\boldsymbol{x}-\boldsymbol{r}_{\alpha\beta})dx_1dx_2$$
$$-\frac{k_{in}}{D}\sum_{\alpha=1}^{2N}\sin\frac{p'\pi x_1}{L_1}\sin\frac{q'\pi x_2}{L_2}\left[\sum_{p=1}^{N_1}\sum_{q=1}^{N_2}(W_{pq\beta}-W_{pq\beta'})\sin\frac{p\pi x_1}{L_1}\sin\frac{q\pi x_2}{L_2}\right]\iint\delta(\boldsymbol{x}-\boldsymbol{r}_{\alpha\beta})dx_1dx_2$$

Using orthogonality of the basis functions and evaluating the integrals in the above equation, we get

$$\left[\frac{1}{\sin^4\theta}(\frac{p'\pi}{L_1})^4+\frac{6}{\sin^2\theta\tan^2\theta}(\frac{p'\pi}{L_1})^2(\frac{q'\pi}{L_2})^2+\frac{1}{\sin^4\theta}(\frac{q'\pi}{L_2})^4+\frac{2}{\sin^2\theta}(\frac{p'\pi}{L_1})^2(\frac{q'\pi}{L_2})^2-\frac{\rho h\omega^2}{D}\right]\sin\theta W_{p'q'\beta}\frac{L_1L_2}{4}$$
$$+\frac{4}{\tan\theta\sin^2\theta}\sum_{p=1}^{N_1}\sum_{q=1}^{N_2}\frac{p\pi}{L_1}\frac{q\pi}{L_2}\left\{(\frac{p\pi}{L1})^2+(\frac{q\pi}{L2})^2\right\}W_{pq\beta}$$
$$\frac{L_1L_2}{\pi^2}\left[\frac{\cos(p-p')\pi}{q-q'}-\frac{\cos(q+q')\pi}{q+q'}\right]\left[\frac{\cos(q-q')\pi}{q-q'}-\frac{\cos(q+q')\pi}{q+q'}\right]$$
$$=-\sum_{\alpha=1}^{14N}\frac{k}{D}\sin\frac{q'\pi r_{\alpha\beta1}}{L_1}\sin\frac{q'\pi r_{\alpha\beta2}}{L_2}\left[\sum_{p=1}^{N_1}\sum_{q=1}^{N_2}W_{pq\beta}\sin\frac{p\pi r_{\alpha\beta1}}{L_1}\sin\frac{q\pi r_{\alpha\beta2}}{L_2}-W_{\alpha\beta}\right]$$
$$-\sum_{\alpha=1}^{2N}\frac{k_{in}}{D}\sin\frac{p'\pi r_{\alpha1}}{L_1}\sin\frac{q'\pi r_{\alpha2}}{L_2}\left[\sum_{p=1}^{N_1}\sum_{q=1}^{N_2}(W_{pq\beta}-W_{pq\beta'})\sin\frac{p\pi r_{\alpha1}}{L_1}\sin\frac{q\pi r_{\alpha2}}{L_2}\right].$$

Rearranging the terms in the above equation and substituting $\theta = 60°$ gives Eq. (18a).

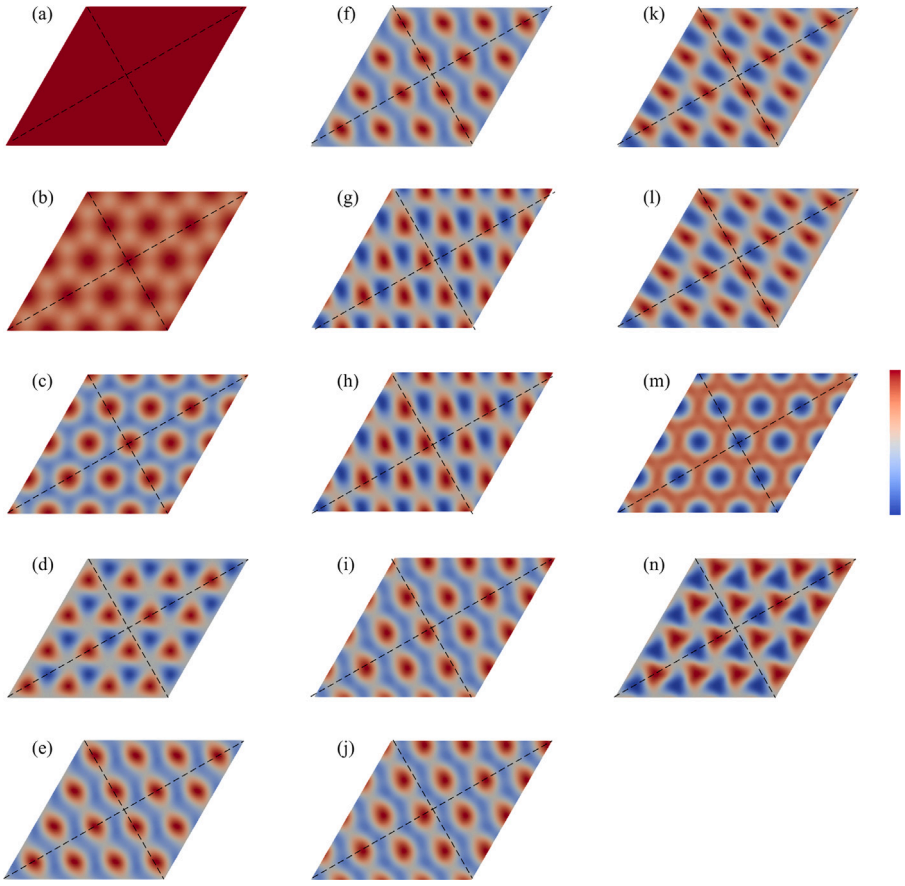

Fig. 11. Nonzero projected Bloch mode shapes under rotation by $\theta = 2\pi/3$ in the top plate at Γ point. Subfigures (a - n) correspond to modes (1–14). Modes having rotational eigenvalue $\lambda_1(p=1)$: $1-4, 13, 14$, $\lambda_2(p=2)$: $5, 7, 9, 11$ and $\lambda_3(p=3)$: $6, 8, 10, 12$. (4×4) unit cells are shown for clarity of rotational symmetry.

For the resonators, substituting the displacements in Eqs. (16) and (17) into their governing equations (7b) gives

$$-m\omega^2 W_{\alpha\beta} = -kW_{\alpha\beta} + k\sum_{p=1}^{N_1}\sum_{q=1}^{N_2} W_{pq\beta}\sin\frac{p\pi r_{\alpha\beta1}}{L_1}\sin\frac{q\pi r_{\alpha\beta2}}{L_2}. \tag{23}$$

Dividing both sides by $-m$ gives Eq. (18b)

Appendix B. Bloch mode shapes

Using the procedure in Section 3.2, the projected Bloch mode shapes $w^p_\beta(\boldsymbol{x})$ for the 14 modes below the band gap are determined at each of the high symmetry points. The non-zero projected mode shapes (real component) are presented in Figs. 9–12. Only the top plate is shown although both plates are considered for determining the rotational eigenvalue λ_p for each mode. The corresponding λ_p for each mode are listed in the captions. Here, multiple unit cells are illustrated for clarity of the rotational symmetry. The rotation axis passes through the center, where the dashed lines intersect. For rotation about this axis by $\theta = \pi$, modes with rotational eigenvalue λ_1 will be symmetric. Similarly, for rotation by $\theta = 2\pi/3$, the mode shapes with λ_1 will be unchanged after rotation.

Appendix C. Primitive generators and their fractional corner modes

We consider two primitive generators, identical to the ones introduced by Hughes and coworkers [22]. Fig. 13(a,c) displays schematics of these lattices. The nodes have point masses with one degree of freedom and can move out-of-plane. The edges have linear springs with stiffness values either k_1 or k_2 as indicated. In both lattices, a nontrivial topological bandgap opens when $k_1 < k_2$. The dispersion diagrams for these lattices, computed for $k_1 = 0.1$, $k_2 = 1.0$ and all unit masses, are displayed in Fig. 13(b,d).

The fractional corner modes at the corners of domains with 6-fold and 3-fold rotation symmetry are given by [22]

$$Q_6 = \frac{[M_1^{(2)}]}{4} + \frac{[K_1^{(3)}]}{6} \mod 1 \tag{24a}$$

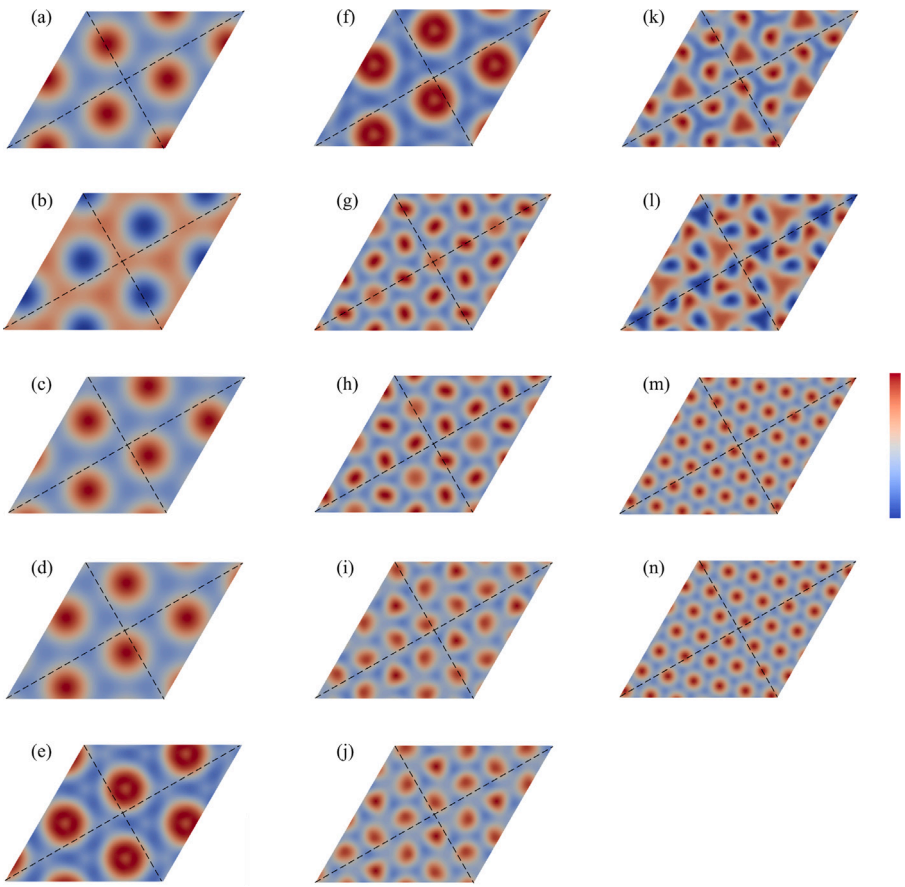

Fig. 12. Nonzero projected Bloch mode shapes under rotation by $\theta = 2\pi/3$ in the top plate at K point. Subfigures (a - n) correspond to modes (1–14). Modes having rotational eigenvalue $\lambda_1(p=1)$: $1, 2, 7, 8$, $\lambda_2(p=2)$: $3, 5, 9, 11, 13$ and $\lambda_3(p=3)$: $4, 6, 10, 12, 14$. (4×4) unit cells are shown for clarity of rotational symmetry.

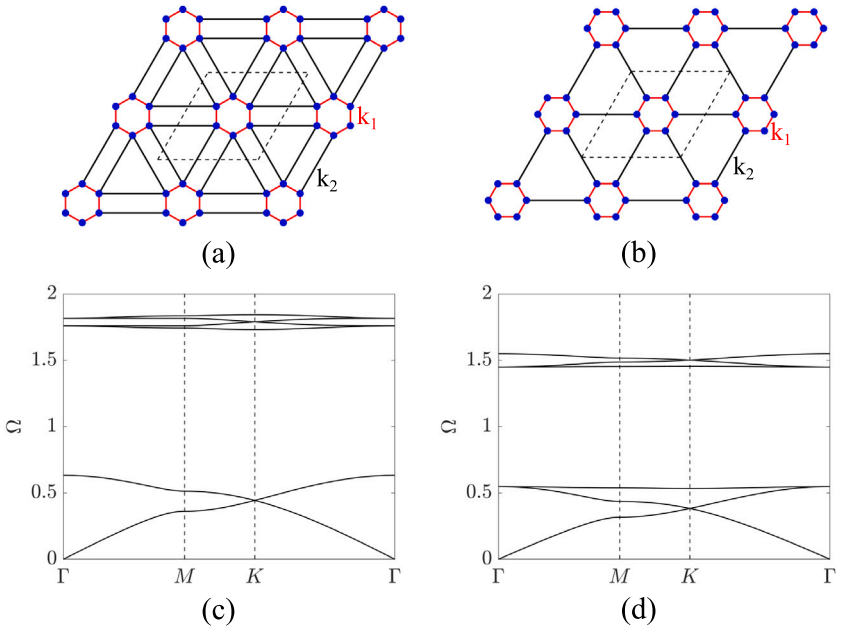

Fig. 13. Schematic and dispersion diagram of the primitive generators. Schematic of (a) h_{4b} and (d) h_{3c} lattices. Unit cells are indicated by black dashed lines. Dispersion diagrams are shown along the IBZ boundary for (c) h_{4b} and (d) h_{3c} lattices.

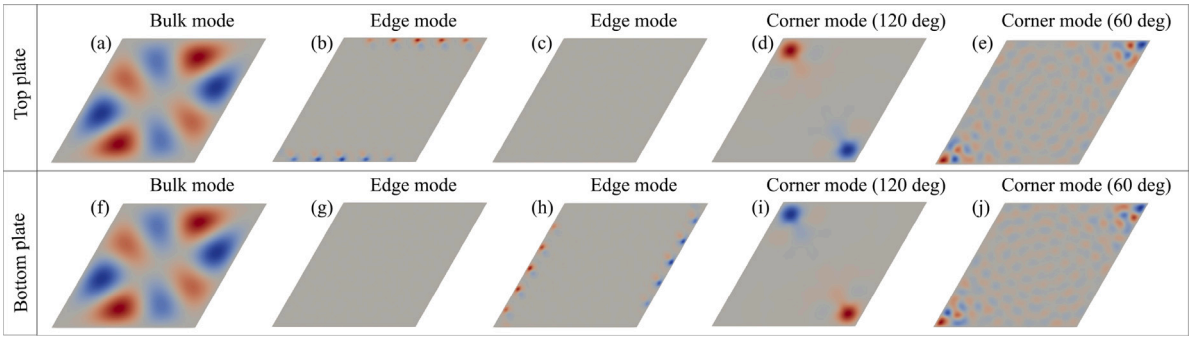

Fig. 14. Displacement contours of top and bottom plate for (a, f) a typical bulk mode ($\Omega = 0.70$), (b, c, g, h) an edge mode ($\Omega = 13.71$), (d, i) corner mode at 120° corner ($\Omega = 2.34$) and (e, j) 60° corner ($\Omega = 8.19$). Top and bottom rows correspond to the top and bottom plate displacement contours, respectively.

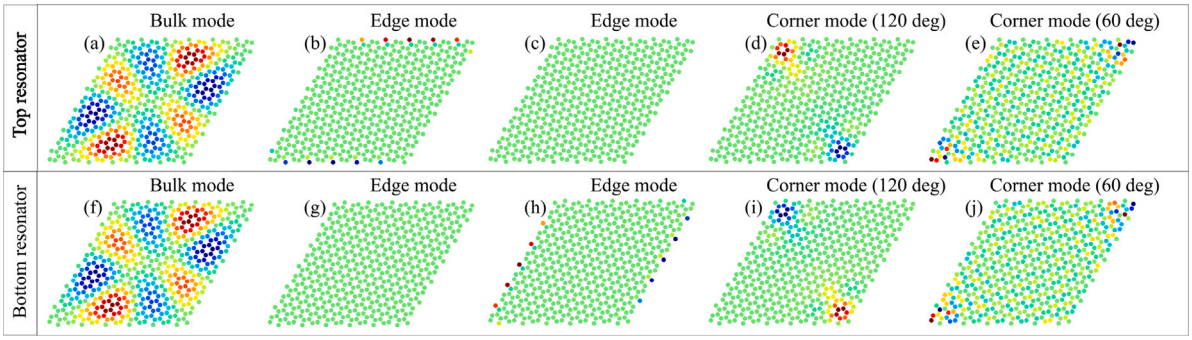

Fig. 15. Displacement contours of top and bottom resonator for the same modes presented in Fig. 14. Top and bottom rows correspond to the top and bottom resonator displacement contours, respectively.

$$Q_3 = \frac{[K_2^{(3)}]}{3} \mod 1. \tag{24b}$$

Here $[K_2^3]$ is the difference between the number of modes at K and Γ points that have rotational eigenvalue λ_2. For each mode at the high symmetry points below the bandgap, the rotational eigenvalues are determined using the procedure discussed in Section 3.2. For h_{4b} lattice, the fractional corner mode values are

$$Q_6 = \frac{(1-1)}{4} + \frac{(0-2)}{6} = -\frac{1}{3} \mod 1 = \frac{2}{3} \mod 1, \tag{25a}$$

$$Q_3 = \frac{(1-0)}{3} = \frac{1}{3} \mod 1, \tag{25b}$$

while for h_{3c} lattice, they are

$$Q_6 = \frac{(1-3)}{4} + \frac{(1-1)}{6} = -\frac{1}{2} \mod 1 = \frac{1}{2} \mod 1 \tag{26a}$$

$$Q_3 = \frac{(1-1)}{3} = 0. \tag{26b}$$

Appendix D. Bulk and localized mode shapes

The complete mode shapes for the modes in Fig. 5 are presented. These include the top and bottom plate displacement contours, top and bottom layer resonator displacement contours. Note that there are two edge modes at the same frequency. Both mode shapes are illustrated below: subfigures (b, g) for one mode and (c, h) for the other.

Appendix E. Supplementary data

Supplementary material related to this article can be found online at https://doi.org/10.1016/j.jsv.2024.118268.

References

[1] J.M.B. Lopes Dos Santos, N.M.R. Peres, A.H. Castro Neto, Graphene bilayer with a twist: Electronic structure, Phys. Rev. Lett. 99 (25) (2007) 256802.
[2] G Trambly de Laissardière, Didier Mayou, Laurence Magaud, Localization of Dirac electrons in rotated graphene bilayers, Nano Lett. 10 (3) (2010) 804–808.
[3] E Suárez Morell, JD Correa, P Vargas, M Pacheco, Z Barticevic, Flat bands in slightly twisted bilayer graphene: Tight-binding calculations, Phys. Rev. B 82 (12) (2010) 121407.
[4] Rafi Bistritzer, Allan H. MacDonald, Moiré bands in twisted double-layer graphene, Proc. Natl. Acad. Sci. 108 (30) (2011) 12233–12237.
[5] Z.F. Wang, Feng Liu, M.Y. Chou, Fractal Landau-level spectra in twisted bilayer graphene, Nano Lett. 12 (7) (2012) 3833–3838.
[6] Yuan Cao, Valla Fatemi, Shiang Fang, Kenji Watanabe, Takashi Taniguchi, Efthimios Kaxiras, Pablo Jarillo-Herrero, Unconventional superconductivity in magic-angle graphene superlattices, Nature 556 (7699) (2018) 43–50.
[7] Luis A Gonzalez-Arraga, JL Lado, Francisco Guinea, Pablo San-Jose, Electrically controllable magnetism in twisted bilayer graphene, Phys. Rev. Lett. 119 (10) (2017) 107201.
[8] Kaichen Dong, Tiancheng Zhang, Jiachen Li, Qingjun Wang, Fuyi Yang, Yoonsoo Rho, Danqing Wang, Costas P Grigoropoulos, Junqiao Wu, Jie Yao, Flat bands in magic-angle bilayer photonic crystals at small twists, Phys. Rev. Lett. 126 (22) (2021) 223601.
[9] Xin-Rui Mao, Zeng-Kai Shao, Hong-Yi Luan, Shao-Lei Wang, Ren-Min Ma, Magic-angle lasers in nanostructured moiré superlattice, Nature Nanotechnol. 16 (10) (2021) 1099–1105.
[10] Mourad Oudich, Guangxu Su, Yuanchen Deng, Wladimir Benalcazar, Renwen Huang, Nikhil JRK Gerard, Minghui Lu, Peng Zhan, Yun Jing, Photonic analog of bilayer graphene, Phys. Rev. B 103 (21) (2021) 214311.
[11] Peng Wang, Yuanlin Zheng, Xianfeng Chen, Changming Huang, Yaroslav V Kartashov, Lluis Torner, Vladimir V Konotop, Fangwei Ye, Localization and delocalization of light in photonic moiré lattices, Nature 577 (7788) (2020) 42–46.
[12] Shi-Qiao Wu, Zhi-Kang Lin, Bin Jiang, Xiaoxi Zhou, Zhi Hong Hang, Bo Hou, Jian-Hua Jiang, Higher-order topological states in acoustic twisted moiré superlattices, Phys. Rev. A 17 (3) (2022) 034061.
[13] Shengjie Zheng, Jie Zhang, Guiju Duan, Zihan Jiang, Xianfeng Man, Dejie Yu, Baizhan Xia, Topological network and valley beam splitter in acoustic biaxially strained moiré superlattices, Phys. Rev. B 105 (18) (2022) 184104.
[14] Simon Yves, Yu-Gui Peng, Andrea Alù, Topological lifshitz transition in twisted hyperbolic acoustic metasurfaces, Appl. Phys. Lett. 121 (12) (2022) 122201.
[15] Yabin Jin, Wan Wang, Zhihui Wen, Daniel Torrent, Bahram Djafari-Rouhani, Topological states in twisted pillared phononic plates, Extreme Mech. Lett. 39 (2020) 100777.
[16] María Rosendo López, Fernando Peñaranda, Johan Christensen, Pablo San-Jose, Flat bands in magic-angle vibrating plates, Phys. Rev. Lett. 125 (21) (2020) 214301.
[17] María Rosendo López, Zhiwang Zhang, Daniel Torrent, Johan Christensen, Theory of holey twistsonic media, Commun. Mater. 3 (1) (2022) 99.
[18] Marc Martí-Sabaté, Dani Torrent, Dipolar localization of waves in twisted phononic crystal plates, Phys. Rev. A 15 (1) (2021) L011001.
[19] Mourad Oudich, Yuanchen Deng, Yun Jing, Twisted pillared phononic crystal plates, Appl. Phys. Lett. 120 (23) (2022) 232202.
[20] Simon Yves, Matheus Inguaggiato Nora Rosa, Yuning Guo, Mohit Gupta, Massimo Ruzzene, Andrea Alù, Moiré-driven topological transitions and extreme anisotropy in elastic metasurfaces, Adv. Sci. 9 (13) (2022) 2200181.
[21] Wladimir A. Benalcazar, B. Andrei Bernevig, Taylor L. Hughes, Quantized electric multipole insulators, Science 357 (6346) (2017) 61–66.
[22] Wladimir A. Benalcazar, Tianhe Li, Taylor L. Hughes, Quantization of fractional corner charge in c n-symmetric higher-order topological crystalline insulators, Phys. Rev. B 99 (24) (2019) 245151.
[23] Yuchen Peng, Exian Liu, Bei Yan, Jianlan Xie, Aoqian Shi, Peng Peng, Hang Li, Jianjun Liu, Higher-order topological states in two-dimensional stampfli-triangle photonic crystals, Opt. Lett. 47 (12) (2022) 3011–3014.
[24] Mingxing Li, Yueke Wang, Tian Sang, Hongchen Chu, Yun Lai, Guofeng Yang, Experimental observation of multiple edge and corner states in photonic slabs heterostructures, Photonics Res. 10 (1) (2022) 197–204.
[25] Langlang Xiong, Yufu Liu, Yu Zhang, Yaoxian Zheng, Xunya Jiang, Topological properties of a two-dimensional photonic square lattice without c 4 and m x (y) symmetries, ACS Photonics 9 (7) (2022) 2448–2454.
[26] Hai-Xiao Wang, Li Liang, Bin Jiang, Junhui Hu, Xiancong Lu, Jian-Hua Jiang, Higher-order topological phases in tunable c 3 symmetric photonic crystals, Photonics Res. 9 (9) (2021) 1854–1864.
[27] Shiqiao Wu, Bin Jiang, Yang Liu, Jian-Hua Jiang, All-dielectric photonic crystal with unconventional higher-order topology, Photonics Res. 9 (5) (2021) 668–677.
[28] Matthew Proctor, Paloma Arroyo Huidobro, Barry Bradlyn, María Blanco De Paz, Maia G Vergniory, Dario Bercioux, Aitzol García-Etxarri, Robustness of topological corner modes in photonic crystals, Phys. Rev. Res. 2 (4) (2020) 042038.
[29] Tomonari Mizoguchi, Yoshihito Kuno, Yasuhiro Hatsugai, Square-root higher-order topological insulator on a decorated honeycomb lattice, Phys. Rev. A 102 (3) (2020) 033527.
[30] Zhenyu Wang, Houyin Li, Zhennan Wang, Zhenzhen Liu, Jinlong Luo, Jian Huang, Xiaoyan Wang, Rongli Wang, Hai Yang, Straight-angled corner state in acoustic second-order topological insulator, Phys. Rev. B 104 (16) (2021) L161401.
[31] Yuanchen Deng, Wladimir A Benalcazar, Ze-Guo Chen, Mourad Oudich, Guancong Ma, Yun Jing, Observation of degenerate zero-energy topological states at disclinations in an acoustic lattice, Phys. Rev. Lett. 128 (17) (2022) 174301.
[32] Zhang-Zhao Yang, Xin Li, Yao-Yin Peng, Xin-Ye Zou, Jian-Chun Cheng, Helical higher-order topological states in an acoustic crystalline insulator, Phys. Rev. Lett. 125 (25) (2020) 255502.
[33] Haoran Xue, Yahui Yang, Fei Gao, Yidong Chong, Baile Zhang, Acoustic higher-order topological insulator on a kagome lattice, Nat. Mater. 18 (2) (2019) 108–112.
[34] Xiang Ni, Matthew Weiner, Andrea Alu, Alexander B Khanikaev, Observation of higher-order topological acoustic states protected by generalized chiral symmetry, Nat. Mater. 18 (2) (2019) 113–120.
[35] Marc Serra-Garcia, Valerio Peri, Roman Süsstrunk, Osama R Bilal, Tom Larsen, Luis Guillermo Villanueva, Sebastian D Huber, Observation of a phononic quadrupole topological insulator, Nature 555 (7696) (2018) 342–345.
[36] Motohiko Ezawa, Higher-order topological insulators and semimetals on the breathing kagome and pyrochlore lattices, Phys. Rev. Lett. 120 (2) (2018) 026801.
[37] Yafeng Chen, Jensen Li, Jie Zhu, Topology optimization of quantum spin hall effect-based second-order phononic topological insulator, Mech. Syst. Signal Process. 164 (2022) 108243.
[38] Chun-Wei Chen, Rajesh Chaunsali, Johan Christensen, Georgios Theocharis, Jinkyu Yang, Corner states in a second-order mechanical topological insulator, Commun. Mater. 2 (1) (2021) 62.
[39] Hrishikesh Danawe, Heqiu Li, Hasan Al Ba'ba'a, Serife Tol, Existence of corner modes in elastic twisted kagome lattices, Phys. Rev. B 104 (24) (2021) L241107.
[40] Ze Ma, Yang Liu, Yu-Xin Xie, Yue-Sheng Wang, Tuning of higher-order topological corner states in a honeycomb elastic plate, Phys. Rev. A 19 (5) (2023) 054038.

[41] Yijie Liu, Boqing Lei, Peng Yu, Lei Zhong, Kaiping Yu, Ying Wu, Second-order topological corner states in two-dimensional elastic wave metamaterials with nonsymmorphic symmetries, Mech. Syst. Signal Process. 198 (2023) 110433.
[42] Bing Liu, Lede Xian, Haimen Mu, Gan Zhao, Zhao Liu, Angel Rubio, ZF Wang, Higher-order band topology in twisted moiré superlattice, Phys. Rev. Lett. 126 (6) (2021) 066401.
[43] Raj Kumar Pal, Massimo Ruzzene, Edge waves in plates with resonators: an elastic analogue of the quantum valley hall effect, New J. Phys. 19 (2) (2017) 025001.
[44] Yong Xiao, Jihong Wen, Xisen Wen, Flexural wave band gaps in locally resonant thin plates with periodically attached spring–mass resonators, J. Phys. D: Appl. Phys. 45 (19) (2012) 195401.
[45] Daniel Torrent, José Sánchez-Dehesa, Acoustic analogue of graphene: observation of Dirac cones in acoustic surface waves, Phys. Rev. Lett. 108 (17) (2012) 174301.
[46] M. Zahid Hasan, Charles L. Kane, Colloquium: topological insulators, Rev. Modern Phys. 82 (4) (2010) 3045.
[47] Christopher W Peterson, Tianhe Li, Wladimir A Benalcazar, Taylor L Hughes, Gaurav Bahl, A fractional corner anomaly reveals higher-order topology, Science 368 (6495) (2020) 1114–1118.
[48] Christopher Bradley, Arthur Cracknell, The Mathematical Theory of Symmetry in Solids: Representation Theory for Point Groups and Space Groups, Oxford University Press, 2010.
[49] Mildred S. Dresselhaus, Gene Dresselhaus, Ado Jorio, Group Theory: Application to the Physics of Condensed Matter, Springer Science & Business Media, 2007.
[50] Stephen Timoshenko, Sergius Woinowsky-Krieger, et al., Theory of Plates and Shells, volume 2, McGraw-hill New York, 1959.